

TERAHERTZ SPECTROSCOPIC IMAGING

by

WILLIAM ELIJAH BAUGHMAN

SEONGSIN MARGARET KIM, COMMITTEE CHAIR

PATRICK KUNG
EDWARD SAZONOV
KEITH WILLIAMS

A THESIS

Submitted in partial fulfillment of the requirements
for the degree of Master of Science
in the Department of Electrical and Computer Engineering
in the Graduate School of
The University of Alabama

TUSCALOOSA, ALABAMA

2014

Copyright William Elijah Baughman 2014
ALL RIGHTS RESERVED

ABSTRACT

Terahertz based imaging techniques are of critical importance in furthering both our understanding of physical laws and the technological ability to observe and diagnose the condition of organic compounds. In this work I present the development of spectroscopic image construction and analysis techniques utilizing Terahertz Time Domain Spectroscopy. LabVIEW has been used to develop a powerful, user-friendly image analysis suite specialized for this purpose. Here I discuss the techniques and methodologies that allow for meaningful color contrast image reconstruction via the extraction of selected criterion from the spectrum associated to a spatial location within a sample.

After the methodology has been presented, I will present a sequence of images captured using the spectrometer. The materials imaged are divided into two categories: inorganic and organic. Through a multitude of reconstructions for each sample, the capability and validity of both THz spectroscopic images and the techniques used to interpret them will be demonstrated.

DEDICATION

This work is dedicated to Julia. The long hours, fatigue, and uncertainty would have long since consumed me without her support and understanding. She has made this work possible, and has remained my light at the end of the tunnel.

ACKNOWLEDGEMENTS

There are a lot of people to thank, and paper is a precious resource so I will keep it short. Most of you know who you are and which category you fall under, so please forgive me for not listing you by name – be assured that your contributions have not gone unnoticed.

First, I would like to thank my advisors (Dr. Kim and Dr. Kung) for giving me the opportunity to research and providing guidance and support, and of course the members of my committee for taking time to assess the validity and merits of my work. I would also like to thank my fellow group members for their constant encouragement and help. A particular thanks to Tunde for laying the groundwork capabilities of our imaging system and Shawn (my ‘partner in crime’) who was there for all of the long hours and technical difficulties. And a thank you goes out to all the funding sources who kept me fed, and kept the lasers running while I buried my head in work.

Finally to my friends and family, you provided the reasons that drove me to become more than what I was and without that I would have never know the heights to which I can someday rise.

CONTENTS

ABSTRACT.....	ii
DEDICATION.....	iii
ACKNOWLEDGEMENTS.....	iv
LIST OF FIGURES	vii
CHAPTER 1: INTRODUCTION.....	1
1.1 Background and Objectives	1
1.2 Organization.....	1
CHAPTER 2: TERAHERTZ RADIATION.....	4
2.1 History of Terahertz.....	4
2.2 Characteristics of Terahertz Radiation.....	6
2.3 Applications of Terahertz Technologies.....	7
2.3.1. General Applications and Research Areas of Terahertz Technologies	7
2.3.2 Conventional Biomedical Imaging	8
2.3.3 Survey of Terahertz Biomedical Imaging.....	11
CHAPTER 3: EXPERIMENTAL DESCRIPTION.....	13
3.1 THz-TDS System Description	13
3.1.1 THz Generation.....	14
3.1.2 Propagation Path and Sample Orientation	15
3.1.3 Electro-optic Detection	16
3.2 THz Waveform Acquisition.....	17
3.3 Image Acquisition Method	20
3.4 Zero Padding of Time Domain Data.....	22
CHAPTER 4: LABVIEW SOFTWARE DEVELOPMENT.....	24
4.1 Introduction.....	24
4. 2 Operation of the Terahertz Analyzer	26
4.2.1 Initial Loading and Formatting of Image Data	28

4.2.2 Selection and Display of Images.....	30
4.2.3 Image Enhancement.....	32
4.2.4 Image Inspection Tools.....	36
4.3 Image Reconstruction Methods	39
4.3.1 Basic Time Domain Reconstructions.....	39
4.3.2 Time Domain Derivative Imaging	42
4.3.3 Frequency Domain Image Construction	43
4.3.4 Advanced Image Reconstruction Methods	45
CHAPTER 5: INORGANIC IMAGE RECONSTRUCTION.....	48
5.1 Sample Description and Experimental Details	48
5.2 Results and Discussion	50
5.2.1 Time Domain Reconstruction	50
5.2.2 Frequency Domain Reconstruction.....	52
CHAPTER 6: IMAGING OF BIOLOGICAL SAMPLES	55
6.1 Osseous Tissue Identification	55
6.1.1 Sample Preparation and Experimental Parameters	55
6.1.2 Time Domain Analysis	57
6.1.3 Frequency Domain Analysis.....	61
6.2 Observation of Structural Damage in Cartilage Tissue	64
6.2.1 Sample Preparation and Experimental Parameters	64
6.2.2 Image Analysis and Discussion	66
6.3 Comparison of Structural Damage on Fixed vs. Un-fixed Tissue	68
6.3.1 HF Burn on Formalin Fixed Osseous Tissue.....	69
6.3.2 HF Burn on Un-Fixed Osseous Tissue	73
6.3.3 Comparison of Results from Fixation.....	79
CHAPTER 7: CONCLUSION	81
REFERENCES	83

LIST OF FIGURES

Figure 1. The terahertz gap within the electromagnetic spectrum [13].	5
Figure 2. Visual comparison of the size of common objects with wavelength as well as the photon energy and chemical bond energy in the terahertz region (shaded) [13].	7
Figure 3. Schematics of the THz-TDS used for this work.....	13
Figure 4. Photoconductive antenna design and operation	14
Figure 5. Diagram of electro-optic balanced detection.....	16
Figure 6. Typical time domain THz pulse from the system.	17
Figure 7. a) TD waveform and b) amplitude spectrum as sample rate decreases.....	19
Figure 8. a) TD waveform and b) amplitude spectrum as the Time Domain window changes. ..	20
Figure 9. Image raster method for fast and regular image acquisition.	21
Figure 10. Zero-padded (red) vs. Non-padded (black) frequency spectrum. Vertical lines indicate data points	22
Figure 11. LabVIEW front panel for the Terahertz Analyzer software. Components of software indicated.....	25
Figure 12. LabVIEW block diagram overview.....	26
Figure 13. LabVIEW programming for the spectroscopy tab including UI and block diagram. .	27
Figure 14. LabVIEW lock Diagram depicting the image loading sequence.	29

Figure 15. Example of a single image rendered a) monochromatically and b) using the color scale.....	31
Figure 16. Effects of Gain on imaging results	33
Figure 17. LabVIEW code for enhancement processes.....	34
Figure 18. Effects of interpolation on an image file	35
Figure 19. Pixel Review interface.....	37
Figure 20. Row and column trend graphs.....	38
Figure 21. Utilization of the pixel cursor to identify pixel data.....	38
Figure 22. Waveform visualization of reconstruction methods.....	39
Figure 23. a) Difference in Peak Amplitude and Peak Absolute Amplitude images, and b) example of a split pixel spectrum	40
Figure 24. LabVIEW Block Diagram for basic time domain pixel extractions	41
Figure 25. LabVIEW Block Diagram for d/dt pixel extractions.	43
Figure 26. Representation of frequency selection for amplitude and phase spectra.....	43
Figure 27. Labview Block Diagram for frequency domain pixel extraction.....	44
Figure 28. LabVIEW block diagram for single and multiple parameter reconstructions.....	46
Figure 29. Time domain peak-to-trough image of microchip using color contrast, interpolated bicubically to 4976 pixels	50
Figure 30. Time domain propagation delay images of microchip using color contrast, interpolated bicubically to 4976 pixels.....	51

Figure 31. Amplitude reconstructions at select frequencies of the microchip using color contrast, interpolated bicubically to 4976 pixels	53
Figure 32. Phase reconstructions at select frequencies of the microchip using color contrast, interpolated bicubically to 4976 pixels	54
Figure 33. a) Picture of chicken femur cross-section with locations of each baseline scan indicated, and b) THz TDS results for each baseline.....	56
Figure 34. Time domain Peak intensity image reconstructions using color contrast for a) unity gain and b) 230% gain	58
Figure 35. Time domain propagation delay image reconstructions using color contrast for a) positive peak and b) peak of the absolute value	59
Figure 36. Time domain fixed delay image reconstructions using color contrast.	60
Figure 37. Frequency power spectrum for characteristic tissue baselines	61
Figure 38. Frequency domain power spectrum image reconstructions at select frequency and integrated over the range using color contrast.	62
Figure 39. Cartilage burned in two locations by 48% and 24% HF.	65
Figure 40. a) TD Amplitude Image, b) propagation delay image, and c) selected TD waveforms from the image data.	67
Figure 41. Power spectrum images at two frequencies a) 0.45 THz, b) 0.7 THz and c) frequency power spectrums for the selected.....	68
Figure 42. Formalin Fixed tissue with HF burn.....	70
Figure 43. Time-domain images construction from a)peak and b)propagation delay.	71

Figure 44. Selected pixel data for a)Time domain b) Frequency Domain from the formalin fixed tissue.	72
Figure 45. Frequency-domain images construction of power spectrum at a) 0.425 THz and b) 0.8 THz	73
Figure 46. a) Tissue before burn and b) Tissue after HF exposure.....	74
Figure 47. a)before burn TD peak, b) before burn delay, c) after HF TD peak, and d) after HF delay	76
Figure 48. Selected pixel data for a)Time domain b) Frequency Domain before and after HF exposure.	77
Figure 49. Power Spectrum images of a) non-burned, b) burned tissue at 0.425 THz; and for c) non-burned, d) burned tissue at 0.8THz.....	78

CHAPTER 1: INTRODUCTION

1.1 Background and Objectives

Previously, our group has applied the Terahertz Time Domain Spectrometer (THz-TDS) presented here to several primary areas of research. First, the spectrometer was modified to incorporate image capturing capability. This allowed for image construction of the THz transmission spectroscopic response for small samples; with a maximum image size of 2cm x 2cm. This modification drastically improved the control and precision of both sample placement and experimental configuration changes to the spectrometer as a direct byproduct of the image capturing method. With the expanded experimental capability in hand, our group has focused on three primary areas of research: semiconductor material analysis [1], imaging of biological systems [2-4], and development of Terahertz frequency metamaterials [6-8].

The purpose of this work is the development of the reconstruction algorithms and analysis techniques necessary to clearly and quickly interpret the imaging results. For this, a LabVIEW toolkit was created that provides a variety of reconstruction methods, image enhancement functions, and spectroscopic analysis tools. Once completed, these reconstruction techniques and analysis tools were applied to a study of both simple inorganic structures and a study of the THz responses of osseous tissues in several conditions.

1.2 Organization

The remainder of this work is divided into 6 chapters. Chapter 2 presents basic introduction and background information. Here I will sketch out a brief explanation of the history of Terahertz radiation along with the potential applications that have been discovered

thus far. The purpose of this is to develop a common perspective on the nature and layout of the research and application fields while simultaneously highlighting the relative novelty of THz based technologies and the challenges that are currently faced. A particular focus will be given to the work that has been done in the area of biomedical imaging; including discussion on existing imaging techniques that do not rely on THz radiation.

The third chapter is devoted to the basic experimental details associated with this work. First, an explanation of the fundamental physical principles of THz-TDS is given that is particularly focused on the operating principles of the source and detector of the specific spectrometer used in this work. Next, the methodology of data acquisition for both single spectroscopic waveforms and image construction is detailed. Finally, chapter 2 discusses the processing used in the Fast Fourier Transforms necessary to generate frequency domain data. Understanding the principles and methods presented in this chapter serves as a critical foundation for both the development of the image analysis software and for the accurate interpretation of data collected using the THz-TDS.

Chapter 4 is devoted to the explanation of the image analysis software which serves as the centerpiece of this thesis. After a brief introduction in LabVIEW – the language used to develop this program – and the reasons for this software selection, the functionality and operational methods of the Terahertz Analyzer suite will be discussed in detail. To conclude this chapter, the algorithmic methods and basic physical interpretation of the image construction criteria selection and extraction will be discussed.

These first chapters lay the groundwork for the understanding and execution of THz-TDS imaging and image construction. With this in place, the next two chapters of this work are devoted to the presentation of experimental results. Chapter 5 presents a simple, inorganic

microchip. The analysis of images for this object provide a straight-forward and largely unambiguous showcase of the image construction methods presented in the previous chapter. There is a two-fold result from the THz imaging of this sample. First, the basic limitations of system sensitivity, spatial resolution, and overall methodology can be assessed. Second, the relative simplicity of the sample provides a frame of reference for the more structurally complex organic samples presented in chapter 6.

The organic samples presented in chapter 6 provide a study performed on osseous tissues. To begin, the tissue types are identified using THz-TDS in a complex sample that includes overlapping regions of different tissues. Imaging was performed and reconstructions were formed based solely on the predictions made from single spectroscopic responses for each tissue type. This was done to confirm that data from an individual scan can characteristically define the behavior; and that the image construction will reflect this behavior.

With this confirmation in hand, the study of osseous tissue extends to distinguishing structural changes within a tissue type. For this, hydrofluoric acid was employed. In this study we observe the change in THz response due to the structural damage with respect to three different cases. The first case is based on the acid concentration; where we expose cartilage tissue for the same duration with two concentration levels and compare the difference in structural change. This concentration study also allows us to select a concentration level to be used for the other two cases; which are exposure for different tissue types (compact bone and cartilage), and exposure for both tissue types when no histological fixation has been applied prior to imaging.

The final chapter of this work is the conclusion, where results and observations are summarized and the overall success and achievements of this work are discussed.

CHAPTER 2: TERAHERTZ RADIATION

2.1 History of Terahertz

One of the first things to understand when discussing the history of Terahertz is that even today there does not exist a single standard definition of which frequencies are included as Terahertz. Terahertz radiation generally refers to wavelengths between $3000\mu\text{m}$ and $30\mu\text{m}$ corresponding to frequencies of 0.1 to 10THz; and it is this definition that will be used from here on in this work. Far Infrared (FIR) is another term that has several potential definitions. For this work, we will define FIR as corresponding to the frequency range of 300 GHz to 20 THz which almost entirely contains the region we refer to as THz.

The first scientific glimpse into the generation and detection of radiation in the far infrared (FIR) region of the electromagnetic spectrum was performed by researchers over a century ago in the 1890's [9, 10]. At the time, however, the technology was inadequate for accurate and efficient generation and detection of radiation at all frequencies within this range. This made any in-depth exploration or utilization of THz unfeasible. Part of this difficulty stems from the fact that the THz region – sometimes referred to as the ‘Terahertz Gap’ – represents the frequency range where our understanding of photon matter interactions transitions from Maxwell’s Equations of electromagnetics to Schrodinger’s interpretation of quantum mechanical systems. At the time there existed neither transistors capable of attaining sufficiently high operating frequencies nor diodes capable of attaining sufficiently low operating frequencies [10-12].

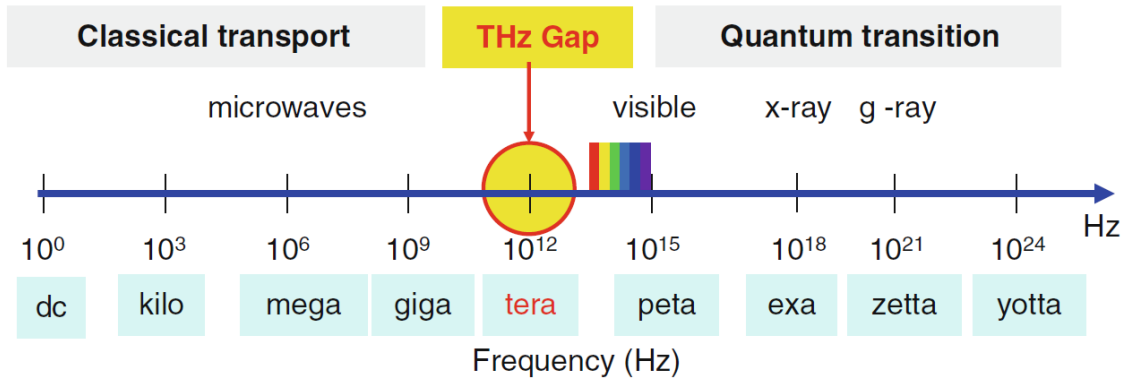


Figure 1. The terahertz gap within the electromagnetic spectrum [13].

In the 1920's, the 'gap' was first bridged with the advent of a Hertzian oscillator which produced 220 μm waves that overlapped with those generated by existing optical techniques [13]. This breakthrough meant that using a combination of sources and detectors from both optical and electronic fields, any individual frequency of radiation within the 'gap' could be successfully generated and detected, with the overlap providing a calibration reference with which the lower and higher frequency spectra could now be successfully joined. This was most notably demonstrated in 1935 with the first recording of the complete water absorption spectrum in the FIR region [14]. Despite these breakthroughs, THz exploration remained elusive due to difficulties of power generation, experimental sensitivity, and the limitations of device fabrication capabilities [15]. These obstacles continue to challenge researchers approaching THz technology from both electrical and optical techniques. In the late 1980's, however, optical rectification and photoconductive techniques were successfully applied in the THz region, thereby introducing the two methods of generation that are most widely used today [17-24]. Many improvements to these technologies have been accomplished through the alteration of antenna geometries and application of different electro-optic or semiconductor materials [25-34]; but there is still room to expand and improve these devices.

Despite the rapid growth of our understanding and technology, manipulation and utilization of THz radiation still lacks the capability that has been obtained for many other portions of the electromagnetic spectrum. To date, a significant portion of the research in this field remains focused on the development of technologies for the generation, detection, and control of THz waves. Due to the nature of the radiation, a wide variety of techniques – optical, electrical, and material – are being explored at an ever increasing rate.

2.2 Characteristics of Terahertz Radiation

There are several important characteristics of THz radiation that, if utilized correctly, can provide a basis for new technologies across a variety of industrial, research, and commercial fields. Terahertz waves are non-ionizing due to the low photon energy (0.4 – 40meV) and are thus capable of harmlessly penetrating many non-conductive materials including most clothing, papers, ceramics and plastics while allowing the spectroscopic response of both these materials and objects beyond or encased within to be detected [35-37]. Another important physical characteristic is that the vibrational modes of numerous molecules, most notably proteins and other biological macromolecules, fall within the Terahertz region. Minute structural changes can be clearly observed in and correlated to changes of THz absorption spectra, making THz spectroscopy a unique characterization technique for sensing organic compounds [38]. Researchers have also used THz spectroscopy to investigate the frequency dependent electrical and optical parameters of materials and devices. Complex index of refraction, complex conductivity, permittivity, and carrier lifetime can be extracted from an object by detailed study of the response (absorption, reflection, and transmission) to THz radiation [39-43]. For these

reasons, the use of THz waves offers many interesting opportunities for research as well as industrial and commercial applications in biology, medicine, chemistry, and physics.

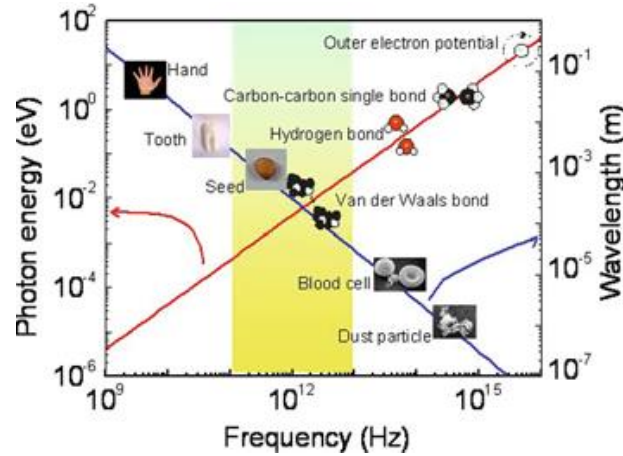


Figure 2. Visual comparison of the size of common objects with wavelength as well as the photon energy and chemical bond energy in the terahertz region (shaded) [13].

2.3 Applications of Terahertz Technologies

2.3.1. General Applications and Research Areas of Terahertz Technologies

Improvements on existing THz generation, detection, and control technologies – as well as the development of new techniques – still comprises the majority of research being performed in this region of the electromagnetic spectrum [37, 44]. The advent of any new devices, however, must go hand in hand with the identification and exploration of real world applications. To that end, and although an increasing number of research areas are being explored as the availability of THz devices continues to expand, there are a few key areas in which THz technologies are primarily focused. Two of these areas, astronomy and communication, will not be discussed here as they do not relate directly to the work performed by our group. It is noted, however, that both of these fields of research are extremely active; and have produced promising

demonstrations of application and developed fundamental technologies that have shaped the fundamental understanding and capability of THz wave behavior and interactions [45-49].

In addition to these two areas, several other primary application fields have been identified across the commercial, industrial, and research sectors. Many of these applications pertain not only to spectroscopy but also to spectroscopic imaging. As mentioned previously, unique identification of complex biomolecules can be accomplished readily with THz radiation and low intensity radiation does not present significant risks of structural damage to the object under study. In addition, the ability to pass through materials allows inspection of the internal structure of an object. These properties have prompted the development of imaging systems by the defense industry for the purpose of security screenings with the aim at full body scanners for contraband detection such as those found in airports [50]. Identification of narcotics, explosive compounds, and other compounds not readily identifiable using conventional sensing has already been demonstrated [51-53]. These same characteristics can be employed for industrial manufacturing and quality/purity screening of organic compounds such as food products, chemicals, and drugs without the need to physically extract samples [54, 55].

2.3.2 Conventional Biomedical Imaging

Imaging in the sense that it is used in the medical field can be defined as the process by which a map is produced based on contrast within the sample that relates to specific criteria. The nature of contrast developed is intrinsic to the modality by which the image is captured and the mechanisms by which both the radiation used (electromagnetic, sonic) interacts with the sample, and is the method by which detection occurs. In general, we can define four main categories of

biomedical imaging that are standard in the medical industry and develop contrast in specific ways. These are imaging based on transmission, emission, reflection, and magnetic resonance [56-60]. Here we will briefly examine the operation of each of these categories through an explanation of the leading technique in each.

The primary technique for both transmission and reflection imaging in the medical industry is x-ray computed tomography, commonly known as CT. In the case of transmission, contrast develops based on the attenuation of radiation as it passes through the subject which leads to tonal contrast rendered through the computation of resulting intensities. Reflection imaging is achieved by receiving the radiation which has been reflected either from the material of the sample itself, or by placing a reflection plane beyond the tissue. X-ray radiation has been in use for so long and has seen such comprehensive study that it has a uniquely well-defined spectral response in typical clinical situations. Furthermore, the flexibility and developments of various reconstruction algorithms for CT have sustained x-ray as the leading diagnostic tool for anatomical studies.

Emissive imaging refers to image contrast developed from the emission of radiation from a subject. The primary area in which emissive imaging has been used is nuclear medicine, which encompasses a host of emissive imaging techniques. In this case it is achieved by introducing radioactive contrast agents such as deoxyfluoroglucose (DFG) to trace physiological and metabolic activity, localizing emitted light.

Another emissive technique is positron Emission Tomography (PET). This technique is most often used in clinical oncological studies. It is achieved by introducing a radioactive biological analogue (often DFG, a glucose analogue) into the body's normal metabolic pathway.

Light is emitted when the tracer decays and positron-electron annihilation occurs, and from this detectable emission image construction is performed.

One of the primary limitations of x-ray imaging techniques is the lack of clearly established contrasts in response to soft tissues. Many techniques have been developed to expand capabilities and overcome this inherent problem [61-64]; however the issue still challenges the scientific community. Soft tissue imaging is of critical importance for medical diagnostics and the techniques of Magnetic Resonance Imaging (MRI) is the primary answer. MRI operates on the principle of nuclear magnetic resonance. In operation, a large magnetic field is applied to the body which produces a spin alignment within the body. The chemical environment of the body's protons determines the frequency of radiation – in the radio wave range – that must be absorbed to allow the protons to come out of the spin-state alignment. Thus by detecting the absorption spectrum of the applicable frequency range, image contrast can be developed.

A wide variety of techniques are currently developed for medical imaging and the place of THz-TDS imaging can be easily identified when the properties of THz biomolecule interaction is understood. THz is unique in that it probes vibrational modes of molecules with motions that extend across a length-scale of tens of angstroms. These length scales correspond to the vibrational modes associated to the conformational states of heme myoglobin and chromophore retinal among others. A protein's effectiveness is directly linked to such conformational states and the ability to spectroscopically observe and identify these states would directly inform the nature of a protein's interactions. This observational ability has far reaching implications not only in diagnosis but also in the determination of disease pathways. Beyond

this, the photon energy levels in the THz region correspond to hydrogen-bonding related interactions.

2.3.3 Survey of Terahertz Biomedical Imaging

The significant first steps in developing commercial grade THz biomedical techniques have already been accomplished across a wide spectrum of applications. The work published to date has focused both on the specific development of spectroscopic analysis of biomolecules and on macro-scale imaging of biosystems.

On the fundamental spectroscopic side of THz biological imaging applications, some of the earliest results began at the turn of the millennium. In 2000, Markelz, Roitberg and Heilweil reported the first use of pulsed THz spectroscopy to examine the vibrational modes of bovine serum albumin and collagen [65]. Shortly thereafter, Brucherseifer et. al reported the first use of Time Resolved THz to observe binding-state dependent properties in polynucleotides which indicated that it would be possible to develop gene probing techniques using THz radiation [66]. Since these initial reports, extensive research has been accomplished in the identification and characterization of biomolecules and the relationship between THz response spectra and molecular structure [67-74]. Additional work in this field has focused specifically on the effects of hydration on the THz spectrum [75, 76].

On the macro scale, impressive studies have been published on the identification of cancer tissue using THz imaging. Although the possibility of cancer detection with THz imaging was suggested nearly 20 years ago [77], the first demonstration of tumor identification via Continuous-Wave Terahertz (CW THz) Imaging was published in 2001 [78]. One year later,

Woodward et. al utilized Terahertz Pulse Imaging (TPI) configured in a reflection geometry to observe skin cancer in humans [79].

Since then several advances have been made in the field of cancer identification with THz. In addition to further observation of cancerous tissue with a refinement of analytical methods and more sophisticated THz systems [80-82], developments of new techniques such as nanoparticle assisted imaging [83] and the advent of specifically designed THz probes [84] have also significantly progressed the field.

Another application of THz imaging to the study of tissue and biological systems has been identified in the field of dentistry. Though not the first to apply THz techniques to dental tissue [85], Pickwell et. al demonstrated that THz imaging techniques can clearly identify the depth and demineralization of tooth enamel [86]. Since this report in 2007, several other groups have continued the investigation into dental applications [87, 88].

Although a plethora of other biomedical imaging applications exist for THz techniques, the final category which has attracted a large interest (and is of particular relevance to this work) is that of osseous tissue investigation. Stringer et. al presented an analysis in 2005 showing a significant correlation between THz-TDS transmission intensity and the density of cortical bone [89]. In addition to these results, initial studies into the detection and monitoring of osteoarthritis using TPI have been published [90, 91]. Three dimensional THz CT has also been used, though penetration depth of the radiation remains a significant challenge [92].

CHAPTER 3: EXPERIMENTAL DESCRIPTION

3.1 THz-TDS System Description

The Terahertz Time Domain Spectrometer (THz-TDS) used for these experiments generates broadband radiation via a photoconductive antenna and detects the resulting radiation with conventional electro-optic sampling. A mode-locked Ti:Sapphire ultrafast laser, at a wavelength of 790 nm, functions as the optical pump for the THz-TDS. This laser, which is used for both emission and detection, supplies 120 mW average power in 120 fs pulses with a repetition rate of 76 MHz into the system. The schematic diagram below depicts the basic operation of the spectrometer, in a transmission regime, that was used for these experiments (Figure 1).

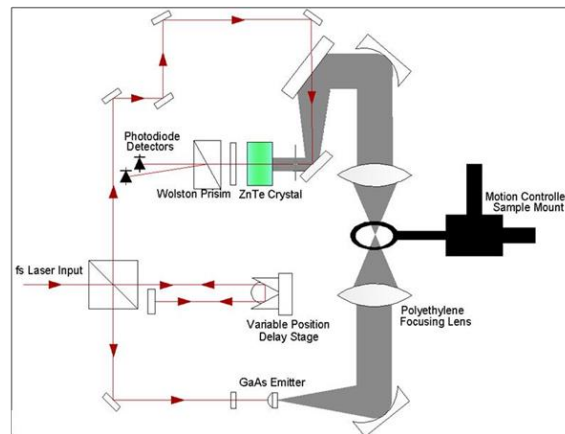


Figure 3. Schematics of the THz-TDS used for this work.

3.1.1 THz Generation

The photoconductive antenna used for THz generation consists of a low-temperature grown GaAs (LT-GaAs) substrate with parallel, gold electrodes. These electrodes form a dipole and are connected to a DC bias which is applied across the antenna at a frequency of 15 kHz. A finger extends from each electrode to form the antenna structure upon which the 790 nm pump laser is focused.

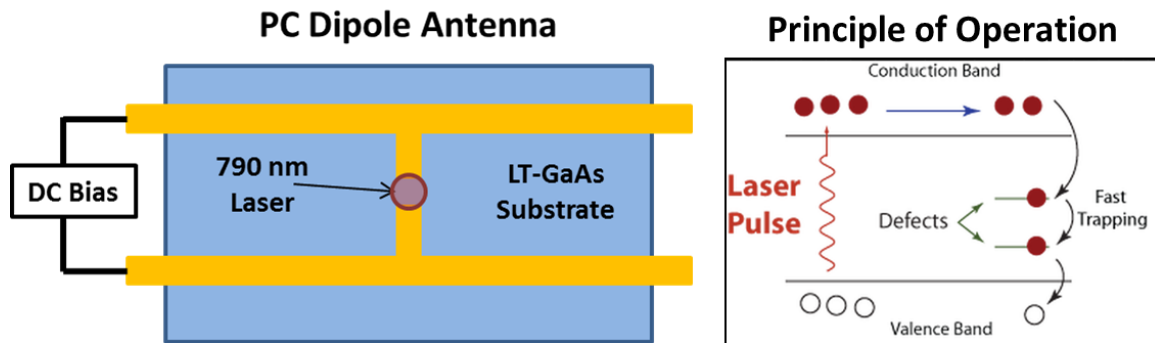


Figure 4. Photoconductive antenna design and operation.

The LT-GaAs is semi-insulating, thus a localization point in the static electric field occurs in the gap between the antenna nodes. The photons of the focused ultrafast pulses from the pump laser exhibit energy ($h\nu$) greater than the bandgap energy of GaAs (1.57 eV vs. 1.42eV), thus electrons are excited from the valence band into the conduction band. Since the applied DC bias creates a static electric field, the photogenerated charge carriers are accelerated across the antenna producing transient surface currents within the LT-GaAs. These moving currents generate a transient electric field that screens the static electric field resulting in a radiated pulse front from the air-semiconductor interface of the antenna. For longer timescales (much larger than the average carrier recombination lifetime), the transient electric field magnitude diminishes due to carrier recombination in the semiconductor and at the contacts. The

static electric field eventually overcomes the decaying transient as the material relaxes to a steady-state (non-excited) [11, 13]. Although several different III-V semiconductors are used for these devices, LT-GaAs is one of the most common. The growth process creates arsenide point defects within the crystal lattice which act as fast traps for the charge carriers allowing for sub-picosecond carrier lifetimes. The material is also ideal for THz generation due to high mobility, resistivity, and breakdown voltage.

3.1.2 Propagation Path and Sample Orientation

The Terahertz pulse is spherically-emitted from the GaAs antenna, focused by a silicon lens, and then reflected from an off-axis parabolic mirror to provide a collimated cylinder of Terahertz radiation. For the transmission regime, a combination of an aluminum plane mirror and a Plano-convex, high density, polyethylene lens – with a focal length of approximately 5cm – is used to focus the beam on the sample down to a spot size of 0.5mm, and a symmetric lens/mirror combination returns the focused Terahertz beam that has transmitted through the material of interest into a cylinder shape for detection. The portion of the 790nm beam used for detection first travels through a variable position delay stage prior to reaching the Terahertz detector. As the delay stage is moved in space, the distance that the probe beam travels is changed on the order of a few millimeters. This additional distance translates into a relative time delay on the order of picoseconds between the terahertz radiation and 790nm pulses.

3.1.3 Electro-optic Detection

The electro-optic detection of THz radiation is achieved by utilizing the change in birefringence, or double refraction, of a ZnTe crystal in the presence of an external electric field, known as Pockel's effect. To realize the small electro-optic effect it is essential that the probe beam from the delay stage and the Terahertz pulse arrive collinearly on the ZnTe crystal. As both beams co-propagate through the birefringent crystal, a phase modulation is induced on the probe beam that causes it to become elliptically polarized in a manner directly proportional to the magnitude of the Terahertz pulse [94]. The horizontal and vertical components of the beam are split with a Wallston prism and sent to two separate photodiodes for balanced detection. The resulting voltage difference is synchronously measured using a lock-in amplifier, at the same gating frequency used for the DC bias applied to the PC antenna, to directly yield the received terahertz electric field intensity. By moving the variable position delay stage, the complete Terahertz waveform can be obtained.

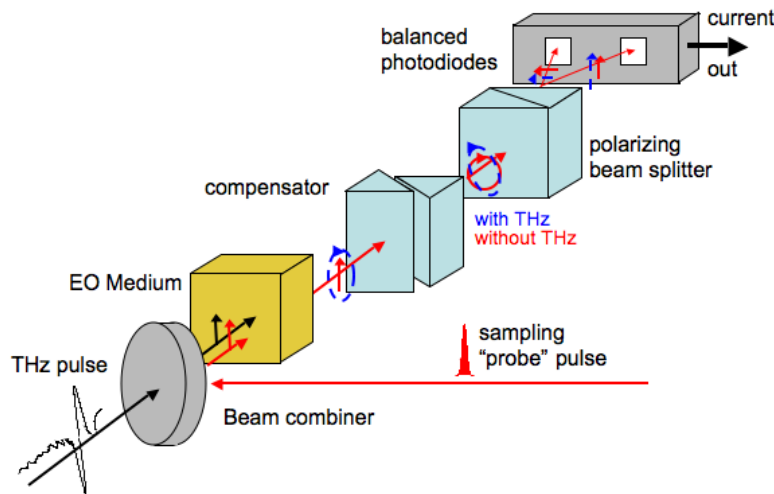


Figure 5. Diagram of electro-optic balanced detection.

3.2 THz Waveform Acquisition

A typical Terahertz time domain pulse obtained from a TDS system is shown in Figure 6. To acquire a THz time domain waveform, the computer control system only requests two pieces of information from the spectrometer: the detected voltage values from the lock-in amplifier and the corresponding position of the delay stage that represents the relative path length that the ultrafast probe beam travels before reaching the detector. From the measured time domain data, the frequency spectra are subsequently obtained by utilizing the Fast Fourier Transform. For the FFT to accurately represent the spectra there are several techniques that must be considered.

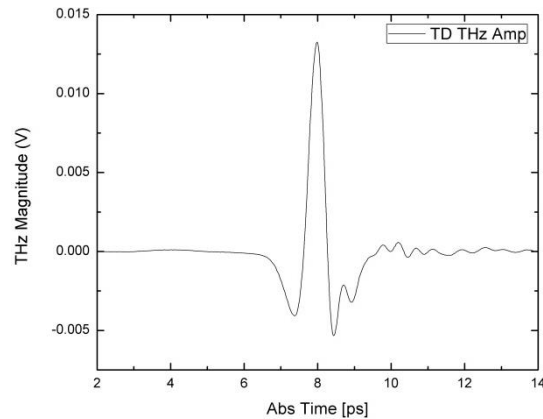


Figure 6. Typical time domain THz pulse from the system.

The acquisition software operates in a polling scheme; that is, it does not request data at specific positions of the delay stage but instead simply requests simultaneous updates as fast as possible. The speed of this is governed by the communication speed of the lock-in amplifier; which is connected via an RS-232 channel. If requests are sent too quickly, the communication with the lock-in times out and data is not received. To overcome this problem, a minimum wait-time is instituted into the controller, and it will not poll position or voltage until the wait-time has

expired. Due to this configuration if the overall scanning velocity is increased it results in a decrease in data density of the captured waveform.

This method of data acquisition results in un-even spacing of points where the resulting time domain data density is a function of the delay stage velocity. To overcome this, linear interpolation of the waveform is performed. The nature of the FFT is such that the spacing of these data points will stretch or compress the frequency spectra. To calibrate this accurately we utilize the narrow water absorption peaks (often referred to as water lines). By interpolating the data such that 1000 evenly spaced data points per 13.3ps (corresponding to 1mm of delay stage motion), the strong absorption lines for the high humidity THz scan align with published values [95].

With the FFT correctly scaled, the next consideration is the obtained frequency resolution. Actual resolution in the frequency spectrum can be improved by simply expanding the window size in the time domain; however, for time windows longer than 20-30ps this method of increasing frequency resolution is no longer practical. There are two main reasons for this, the first being the additional measurement time required. Because of the limitation of device communication speed, increasing the scan window will result in either the loss of time efficiency or a loss in data resolution if the rate of the delay stage movement is increased. Figure 7 shows the change in identical spectroscopic scanning results as the speed of the delay stage is increased. From this, it is observed that both a decrease and shift in the time domain pulse appears to occur when the number of data points per picosecond of time delay is reduced. Additionally, the reduction of time domain resolution results in the loss of smaller variations within the waveform that associate to higher frequency components, thus resulting in an apparent reduction in the amplitude at higher frequencies relative to the amplitude observed at lower.

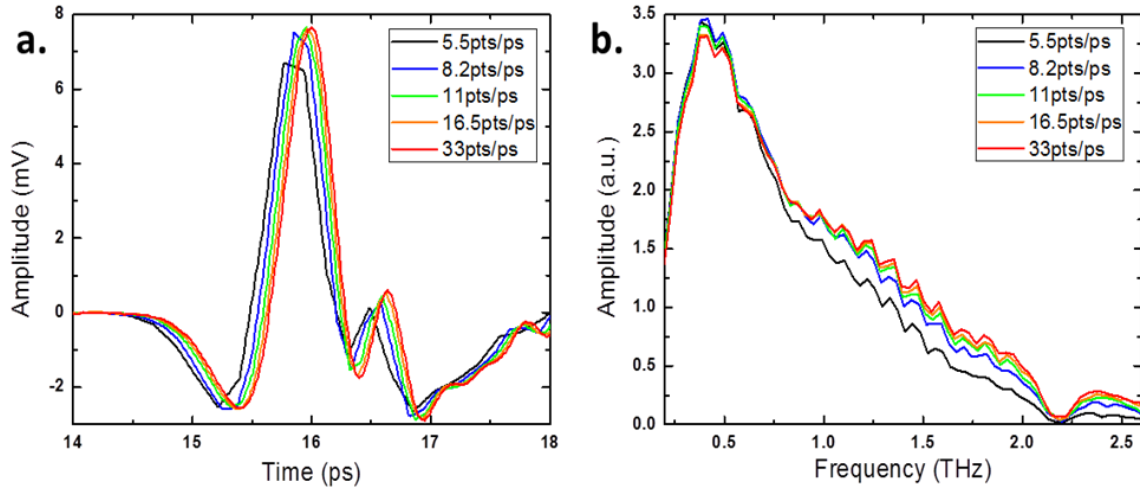


Figure 7. a) TD waveform and b) amplitude spectrum as sample rate decreases.

The second reason that increasing the time domain presents an impractical solution for improving frequency domain resolution is due to the detection of pulse echoes after the initial incidence. The delay of these echoes depends on what types of optics are used to control the terahertz radiation as well as the Fabry-Perot reflections from the sample materials. For the THz-TDS system used here, the first inherent system echo occurs approximately 23ps after the initial pulse. When a sample is placed in the spectrometer; however, the first echo can occur much sooner due to internal reflections of the material as well as the propagation delay caused by the increase in index of refraction of the medium. In the case of a 250um-thick single-side polished silicon wafer, for example, the first pulse reflection is observed 5.3ps delayed from the terahertz wave.

When these pulse reflections are included in the window used for the Fast Fourier Transform, the result is a strong sinusoidal behavior in the amplitude spectrum that can bury small features of the material response. In Figure 8, this sinusoidal result is illustrated by taking a single scan of a bare Si wafer and truncating the scan window at different points to either capture or remove the reflection. For the two transforms which include the reflection, very little

difference can be observed despite the fact that the time range is cut from 26ps down to 11.2ps. However, when the reflection is removed by shortening the window by an additional 1.4ps, the sinusoidal oscillations within the amplitude spectrum disappear. The final curve shows that when the pulse is truncated further below this reflection, actual small features in the spectrum wash out, and only a few dominant frequency behaviors can be observed.

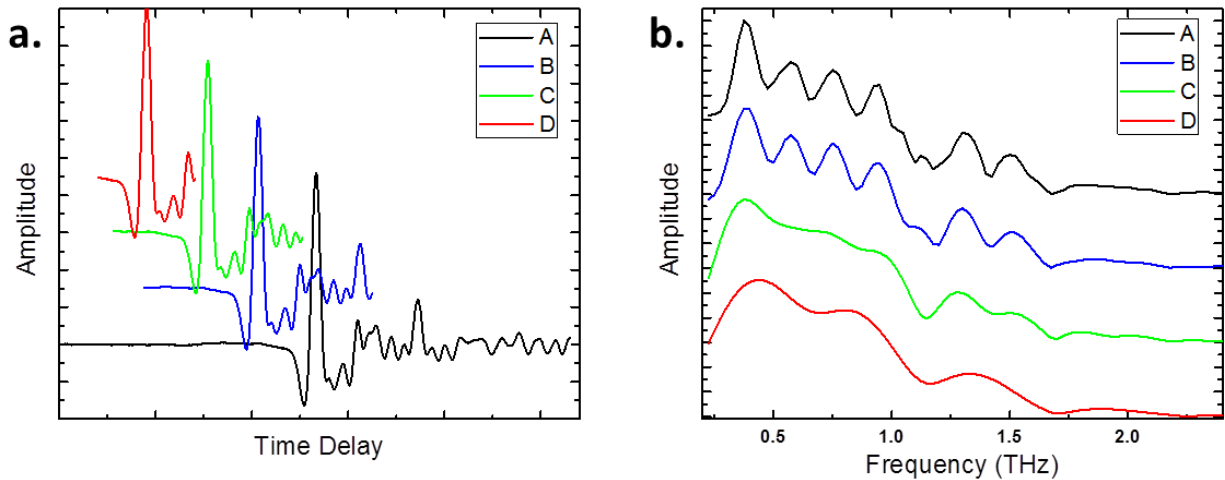


Figure 8. a) TD waveform and b) amplitude spectrum as the Time Domain window changes.

3.3 Image Acquisition Method

To achieve spectroscopic imaging with this system, a three-axis, motion controlled stage is integrated into the sample mount. The motors are positioned such that two of the axes provide translation of the sample in plane with the focal point of the radiation. To capture a two dimensional image, the sample is simply moved in a raster pattern along these two axes with independently defined motion range and step size. For all three axes, the motion controller provides a maximum translation range of 2cm with a minimum repeatable step of 8 μ m.

Two methods are used for image acquisition with this system. The first, referred to as a ‘Fast Image’ holds the optical delay stage at a fixed position and collects a single data point for each pixel corresponding to the intensity of the radiation. For this method, the peak of the THz pulse corresponding to the pixel at the image center position is typically used. With the spectrometer in the transmission regime, this imaging type is used only to position the sample correctly and define the optimum imaging window size.

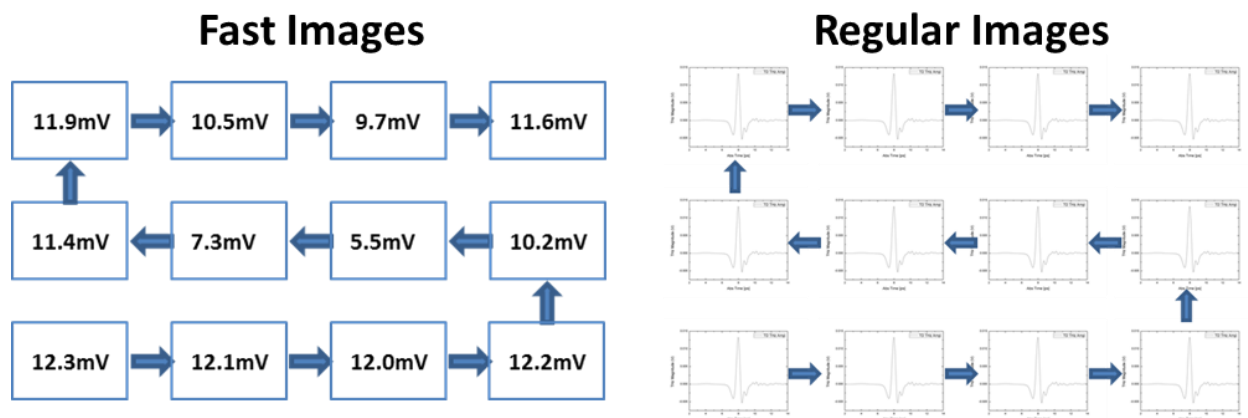


Figure 9. Image raster method for fast and regular image acquisition.

The second method of image acquisition, which will be called a ‘Regular Image’, provides true spectroscopic imaging capability. To obtain a regular image, the sample is held stationary at each pixel position along the raster path while an entire THz-TDS measurement is performed. The scan parameters for each pixel are identical and set during the initialization of the imaging. If movement in the third spatial dimension is desired, the system simply performs imaging in the same method as described. For each position required in the third direction, it repeats the entire imaging process and saves the resulting images separately.

3.4 Zero Padding of Time Domain Data

As the range of the time domain window is decreased, the quantity of points per unit increment in the corresponding frequency spectrum is reduced. Previously, it was stated that for a 40ps time range, the frequency resolution is 0.025 THz, if that window is reduced to, say, the length of curve C in Figure 8, the transformed resolution is reduced to 0.102THz. A simple linear interpolation of the frequency spectrum in this case is not sufficient to resolve any information finer than this; however, zero-padding the time domain signal offers viable insight into features smaller than the resolution limit (Figure 10).

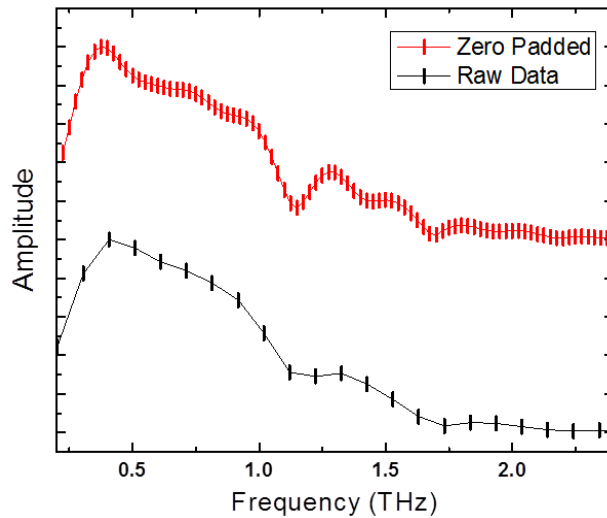


Figure 10. Zero-padded (red) vs. Non-padded (black) frequency spectrum. Vertical lines indicate data points.

By appending data points arbitrarily close to zero on either end of the scan, no new periodic behaviors are introduced into the signal while improving the window size of the time domain signal. This solution does have several drawbacks that should be noted. First, since only a portion of the overall time domain waveform contains meaningful data, the overall amplitude of the spectral features is reduced. This issue can be challenging when attempting to determine small-signal oscillations on a carrier wave in a device situation (such as a radio tower). For

application to terahertz spectroscopic analysis, it is sufficient to verify in the case of any measurements requiring direct comparison that the same data window and zero-padding is used for each scan. If this is not done, the overall amplitude of the spectrums will change. Although the frequencies at which features occur will remain the same provided that the same data window is used and any information corresponding to the relationship of feature amplitudes will be unusable if the zero-padding is not of the same time range.

CHAPTER 4: LABVIEW SOFTWARE DEVELOPMENT

4.1 Introduction

All programming done for this work was completed in National Instruments LabVIEW (Laboratory Virtual Instrument Engineering Workbench). This selection was made based on two factors. First it allows for simple and intuitive development of a custom user interface that allows for active manipulation of the reconstructed images. In addition, future integration with the instrument control software (also developed in LabVIEW) will be possible without fundamental changes in the programming methodology. LabVIEW is a system design software that employs a visual programming language in which the user programs both the operations of the software (in the block diagram) and simultaneously develops a custom graphical user interface (GUI) referred to as the front panel. Programs developed in LabVIEW are called virtual instruments (VIs) and any nested sub-program is referred to as a sub-VI.

When developing or interpreting the operational workflow of the block diagram for a VI, it is important to keep in mind that the software will simultaneously execute as many aspects of the program as possible. For this reason, the employment of structures within the block diagram is critical to achieve the desired operation. The basic structures – case, while, for and event – operate in a fashion that is similar to most other programming environments. The sequence structure is used to force an order of operation into the program that usurps the ordinary flow of the VI. When a sequence is initialized, all processes in each step must be completed before the next step of the sequence is allowed to begin. This is used to prevent the program from

attempting to access a local variable or device before the correct value has been loaded or the communication latency has been allowed to elapse.

The LabVIEW analysis program constructed for this work is a comprehensive software suite designed to allow the user multi-functional image analysis from the THz image data. A separate piece of device-interface software, also developed in LabVIEW, is used to acquire standard THz-TDS spectroscopic data as well as full THz-TDS images. There are two primary objectives that were set to achieve this. First, the program needed to reconstruct contrast images from both the raw and processed data. For this to be successful, the software had to include single spectrum analysis capability and data processing functions such as interpolation, zero-padding and discrete FFT, gain control, and direct image-to-image comparison. Second, the software must provide output capability for both the images and the processed image data (for further analysis in Excel and OriginPro). Figure 11 shows the user interface, or Front Panel, for the LabVIEW suite.

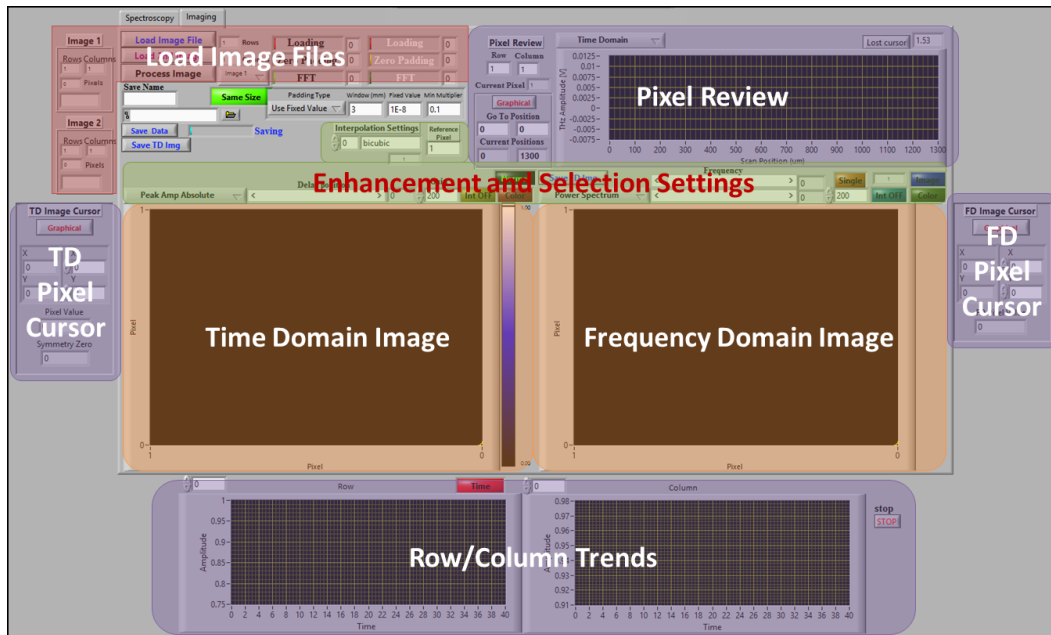


Figure 11. LabVIEW front panel for the Terahertz Analyzer software. Components of software indicated.

4. 2 Operation of the Terahertz Analyzer

The operation of the software can be divided into 6 component areas based on function: initial loading and formatting; selection and display of image; enhancement, inspection, output, and reconstruction techniques. To the extent possible, each component of the program is isolated to minimize the utilization of system resources.

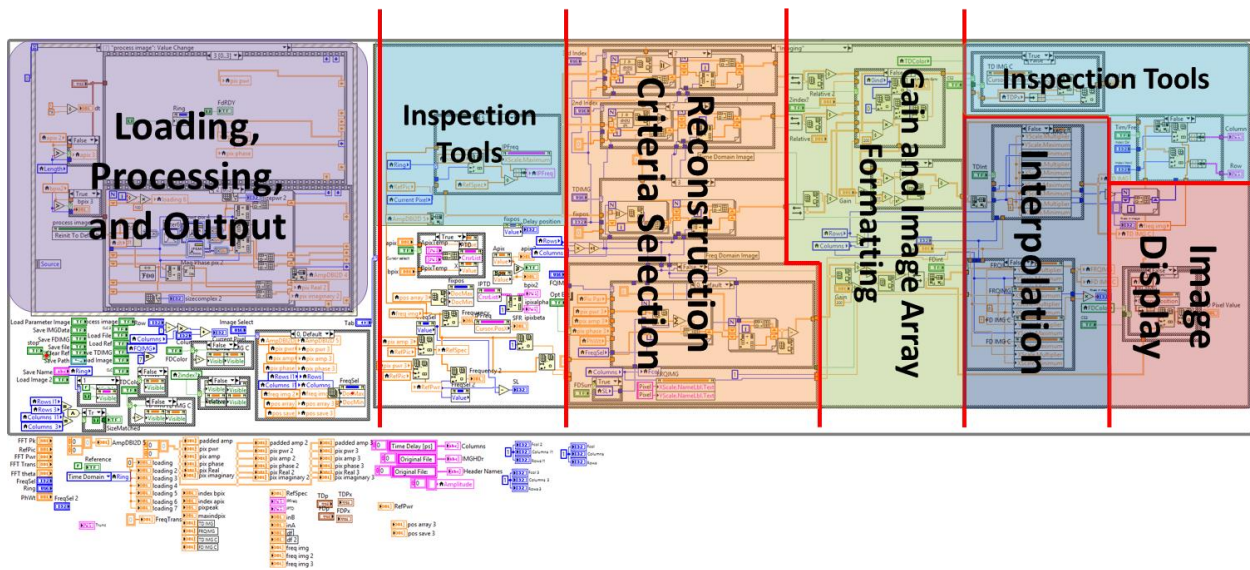


Figure 12. LabVIEW block diagram overview.

The LabVIEW front panel is divided into two separate tabs: Spectroscopy and Imaging. The spectroscopy tab is used to perform basic manipulations – zero padding, FFT, and reference spectrum comparison – of an individual THz-TDS scan. While adjusting the truncation and zero pad settings each step of the process, including the final FFT output, is updated and displayed in real time. Truncation is performed either graphically by sliding two indicator lines on the graph of the initially loaded waveform, or numerically by entering the array row numbers of the desired truncation points. The user is also given the option of viewing either the sample waveform or a separately loaded reference waveform when determining the appropriate settings. This reference

waveform is used to obtain transmission or absorption data by first performing an identical truncation, zero padding, and FFT process as that used for the sample waveform to obtain the frequency dependent amplitude spectrum. The ratio of sample transmission to reference transmission is then obtained by dividing the two spectra. Once all parameters have been satisfactorily set, the results can be output as a text file formatted for easy import into OriginPro.

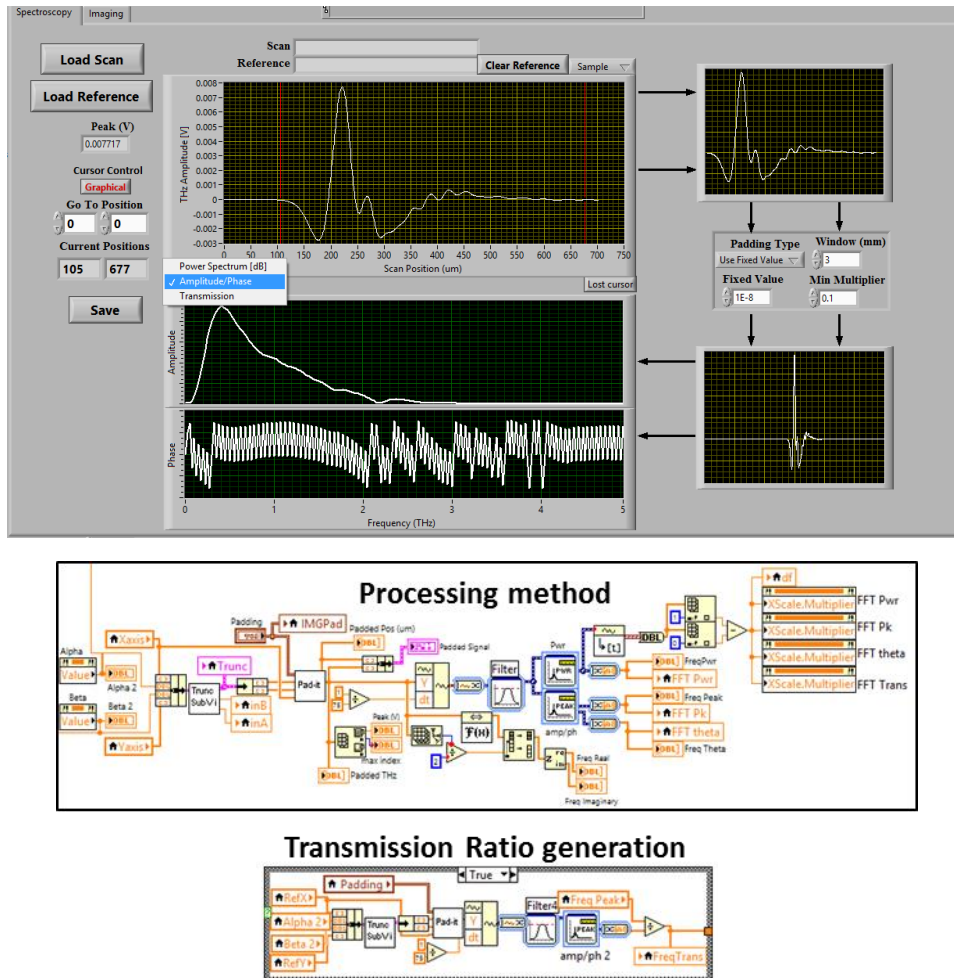


Figure 13. LabVIEW programming for the spectroscopy tab including UI and block diagram.

The imaging tab provides all the functions of image analysis provided by the software for either a single image or two separate image files. The rest of this chapter is devoted to discussion of the image analysis suite. Only the tab currently selected actively utilizes system resources beyond the memory required to store variables.

4.2.1 Initial Loading and Formatting of Image Data

The acquisition software saves image data into a text file by first creating a file with the appropriate experimental parameters in a header, and then appending each new pixel's time domain data in two columns (position and amplitude), as well as a sub-header to indicate the pixel position, to the bottom of the file as it completes the scan for that pixel. In the case of *Regular* images, the acquisition system saves non-interpolated, raw measurement data to minimize file size.

Determinations of the reconstruction method needed and array parameters for the image are made during the initial loading. To extract this information the image file is loaded as an array of strings and from the array three strings are retained: number of rows, number of columns, and image type. The first step the analysis software takes upon loading the file is to determine whether it is a *Fast* or *Regular* image. This is achieved by simple logic comparison on the extracted image type string where true corresponds to a *Regular* and false corresponds to a *Fast* image. Next the numbers corresponding to image size (row count and column count) are then converted to integers and stored for further reference. Finally, the data is reloaded as an array of 32-bit long integers and the header information is discarded.

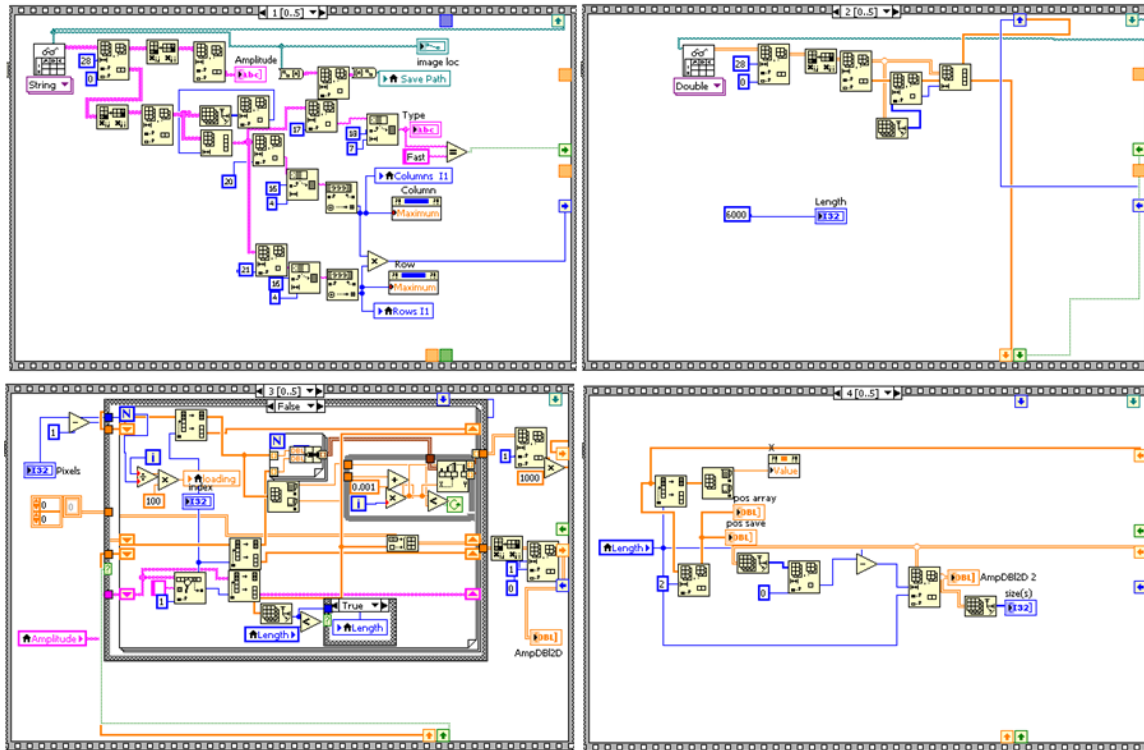


Figure 14. LabVIEW lock Diagram depicting the image loading sequence.

When loading *Regular* images, the input is reorganized from the two column array of data into an array of p columns; where p is equal to the number of pixels in the image. Each column contains only the y -axis values of the spectrum corresponding to a given pixel. Next, the data array is interpolated for each spectrum, column-by-column, using the same interpolation algorithm employed by the acquisition software for basic THz-TDS spectroscopy. A single array is also constructed at this time corresponding to the post-interpolated x -axis values and is used for all pixels, greatly reducing the memory requirement for image processing.

Frequency image construction is also a necessary component of the analysis. As was discussed in the previous chapter, zero padding is used to improve the resolution of frequency data. This is done using the pixel review tools. To generate the frequency data, the user first inspects the time domain waveform of any selected pixel in the image. Sliders on the waveform

allow the data do be truncated where desired. Once the appropriate truncation is set, the user selects the desired zero padding parameters (value and range).

The zero padding determination can be made either on the imaging screen, or on the spectroscopic tab that is designed for single spectrum THz-TDS analysis. The advantage of using the separate tab comes from the fact that for a single spectrum, the software allows a live preview of the frequency domain results based on the current settings. The formatting selected for a single pixel is used for all pixels within the image; therefore it is important to verify that the main THz response for all pixels is within the range when selecting the truncation on an image.

When all selections are complete, the ‘Process Image’ event is activated by the user. This event first zero pads and truncates all pixels of the image sequentially using a simple for loop. Next the software obtains the Fast Fourier Transforms of power, amplitude, and phase for each pixel. Since the Fourier Transform is acquired for all pixels and used to form a new array with column count p equal to the number of pixels, and similarly to the time domain, a single array is used as reference for the x-axis values of all pixel spectrums. The transforms are only recomputed if the user changes any of the truncation parameters and elects to run the transforms again. This drastically decreases the overall computation time required to load each image after the FFT has been completed.

4.2.2 Selection and Display of Images

The same methods for criteria extraction and image construction are used in both the time and frequency images. There are many types of image construction available which will be discussed in a later section. For each type, the software extracts (pixel by pixel) the required

data as a single numeric value and builds the m-by-n array; where m is the number of rows, and n is the number of columns. *Fast* image data is converted directly into the m-by-n array since each pixel contains only one data point. The image acquisition is performed by raster scanning, so every odd numbered row of this array is flipped during the image reconstruction to accurately reflect the spatial position of the pixels.

This 2 dimensional array is then normalized such that the largest valued pixel receives a weight of 1 and is displayed as an intensity graph with the value of each pixel. Two color schemes are used for the contrast scale of the intensity graph. The first is a monochromatic blue scale that transitions from full black to white; and the other utilizes the full color spectrum. These two do not change the value of the pixels within the image; however to visually recognize the region of interest in a sample it may be advantageous to select one over the other. Figure 15 illustrate these two contrast methods. The sample depicted is a simple polypropylene slide with an ‘A’ drawn on it using silver paint.

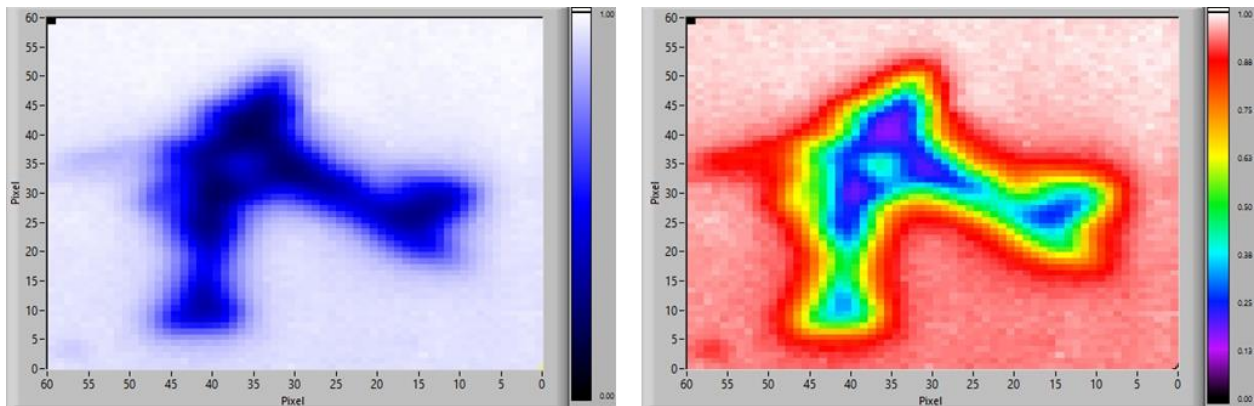


Figure 15. Example of a single image rendered a) monochromatically and b) using the color scale.

4.2.3 Image Enhancement

Before detailing the exact methods of image composition, it is important to understand the methods of image enhancement and inspection that are used. In this toolkit two enhancement techniques are applied: gain and image interpolation. These functions are applied to the final image array after criteria selection is complete. It should be noted that neither of these techniques change the spectroscopic data, but simply change the way the data of each pixel is viewed with respect to every other pixel.

Gain is applied when the pixel values inside of the image (after normalization) are multiplied by a scalar. By effectively controlling gain, relative intensity information for specific regions of a sample can be sharply identified. Figure 16 shows the results of adjusting the gain on the monochromatic image from the previous section. The gain is achieved in the software by applying a scalar multiplication of $g=x/200$, where x is the user specified value and g is the final gain setting, to all pixel values after normalization has been complete. Since the contrast scale only develops for pixel values between 0 and 1, adjusting the scalar gain can highlight different aspects of the image. For the low gain images ($0 < g < 1$), many of the low intensity regions merge together, and only the regions with large differences in intensity are distinguishable. As the gain is increased above unity ($g > 1$), the high intensity regions are pushed off of the contrast scale effectively washing-out the image, and sharp contrasts are detectable among the regions with low overall intensity. The contrast of these low intensity regions is greatly exaggerated. With this kind of basic gain, however, the small variations in regions of high intensity are irresolvable; and when trying to resolve only large differences, the low intensity regions are lost most quickly.

Negative gain can also be utilized, and provides the complementing set of contrast tools. This is achieved simply by defining a negative value of x in the gain equation. After the initial

normalization of the image, the pixel values are inverted such that the highest intensity occurs at 0 and the lowest intensity resolves at the maximum value of the contrast scale. With this, small differences in high intensity regions become clearly resolvable at negative gain above unity ($g < -1$), while suppressing the washing out the lower intensity regions. Similarly, for fractional negative gain ($0 < g < -1$), only large contrast is observable, although this is weighted towards the lower intensity regions of an image.

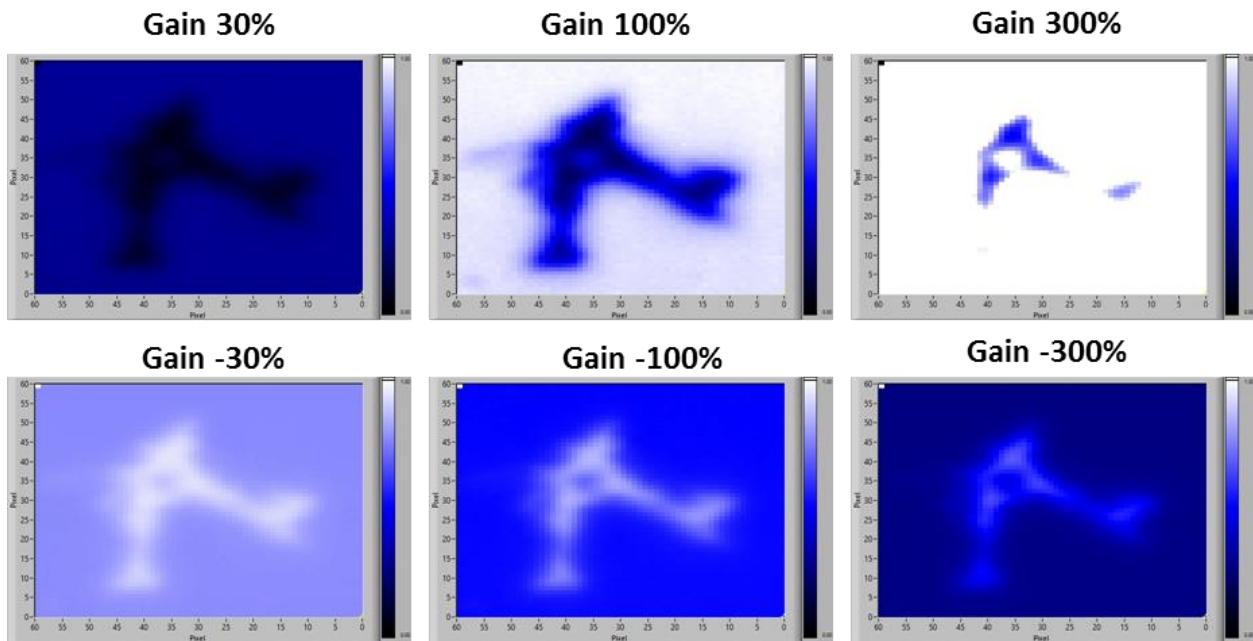


Figure 16. Effects of Gain on imaging results.

By effectively employing this basic form of gain, specific characteristics of the THz response to a sample can be easily visually identified. Applying non-unity gain in any situation does provide a skewed representation of the actual behavior, and therefore to accurately interpret any reconstructed image, it is imperative that the type and severity of the gain used is taken into account. For further images presented here, gain is set to unity unless otherwise noted.

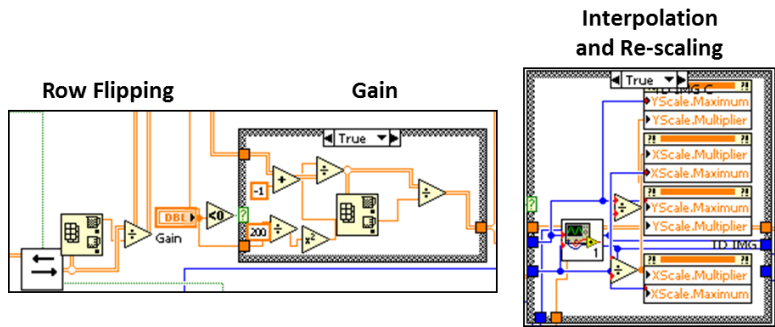


Figure 17. LabVIEW code for enhancement processes.

The next image enhancement technique that the software employs is image interpolation. Applying interpolation to the entire image means that the overall pixel count is increased by adding intermediate pixels between the existing data points. Four methods of interpolation are available in the default LabVIEW libraries; nearest-neighbor, bilinear, bicubic, and bicubic spline. Nearest-neighbor interpolation simply fills in the regions between each data point with the value of the nearest point to the interpolated location. Because of this, it is not useful for enhancing the images that are constructed in the way described here and will not be used in further image analysis. The interpolation of a small image region is shown in Figure 18. Each of the interpolated images shown here contains four times the number of pixels as the original image. The number of total pixels increases by a factor of 4 for each additional interpolation applied. Once the data file is interpolated, the image must be re-scaled to the correct size.

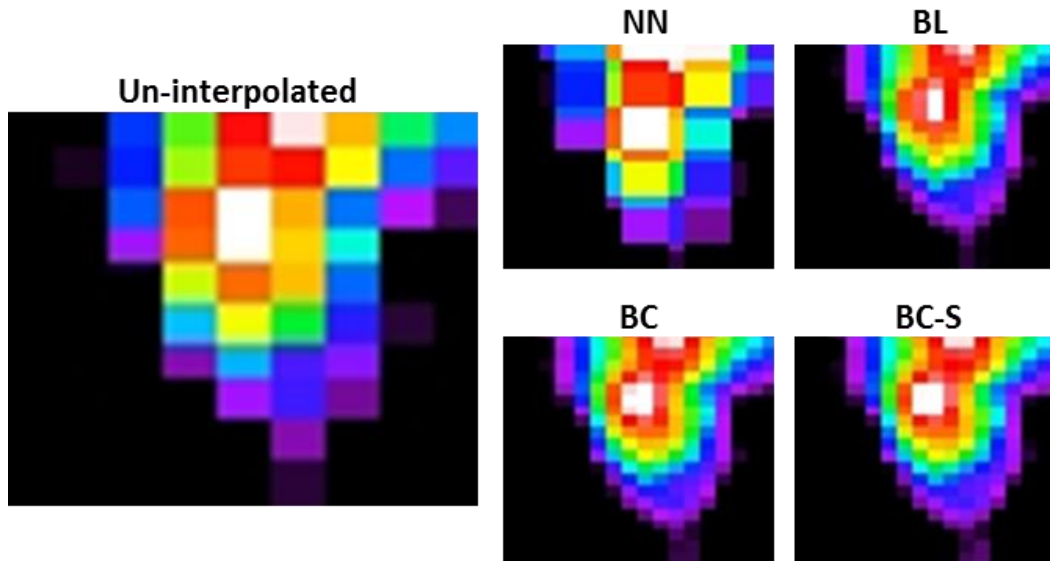


Figure 18. Effects of interpolation on an image file.

The first form of image interpolation that we apply, bilinear (BL), is the fastest interpolation method for improving the quality of the terahertz images. Bilinear interpolation works by first performing a linear interpolation in the horizontal direction, and next performing the same interpolation in the vertical direction. The drawbacks to bilinear interpolation are apparent in the case of a square of four points. The newly interpolated points that lie in the pre-existing rows and columns are simply the point linearly in-between. The point that now lies at the center of the square, however, is the interpolation of two interpolated points, and does not take into consideration the diagonal relationship. In other words, it is an average of two averages. This becomes a significant problem when a large number of interpolated points need to be obtained.

Bicubic interpolation (BC) takes much longer to compute, but yields fewer ‘artifacts’ of the interpolation process. To bicubically interpolate the value, the first derivative in the vertical and horizontal directions and the mixed second derivative with respect to both directions are known; the interpolated data points result from the solution of the coefficients for third degree

polynomial. This ensures that the derivatives are continuous through the interpolated points. The resulting interpolated image is much smoother than the standard bilinear and does not have as many accumulated inaccuracies in the interpolated points.

The difference between the bicubic and bicubic spline (BC-S) interpolation methods is simple. For the basic bicubic, the interpolation solves the image piecewise in small 16 data point rectangles. For bicubic spline, the system performs a 1 dimensional cubic interpolation over each row and then each column and ensures only that the first and second partial derivatives are continuous. This method takes significantly longer than the basic bicubic interpolation. Also, for the requirements of terahertz imaging, this level of continuity is not necessary since the rows and columns are not continuous waveforms over the entire range of the image.

Interpolation as it is used for our purposes is purely to facilitate the user interpretation of patterns within the image via the reduction of pixelization, and comes at the expense of software performance. Increasing the level of interpolation drastically increases the time required to load or reload an image after changing criteria selection and gain. Thus, high factors of interpolation are both unnecessary and impractical.

4.2.4 Image Inspection Tools

There are also three inspection tools available: pixel data view, row and column trends and the pixel selection cursor. The use of all three of these inspection tools is interconnected both with the selection and identification of desired image constructions and with the use of each other. Although significant information can be determined with these tools, it should be noted

that they are not designed to substitute for the use of other software such as OriginPro or Excel for spectroscopic analysis.

The first of these, pixel data view, has been alluded to when discussing the zero padding process. Within the imaging tab, a graph is presented which displays the data from a selected pixel (Figure 19). This pixel view can be used not only to perform the truncation before completing the FFT, but can also be used to represent a variety of time domain and frequency domain graphs based on the pixel. All graph options correspond to the available reconstruction methods within the software. In addition, a separate cursor (the yellow line on the graph in Figure 19) is available with the frequency plots which allows the user to highlight a feature, determine the frequency at which that feature occurs, and use it for the frequency domain image constructions.

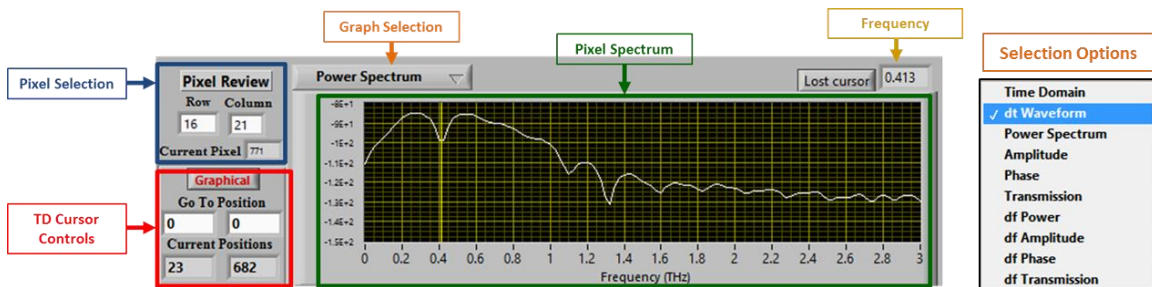


Figure 19. Pixel Review interface.

The next inspection tool provided by the software is the row/column trend graphs. These plots show the pixel values across the row and column indicated for the displayed image (either time or frequency). This feature facilitates the determination of height, width, and separation of features within the sample. For this work, the primary application of these trend graphs was for the alignment and location of the image window and path of terahertz propagation; as well as accurate determination of beam spot-size at the sample.

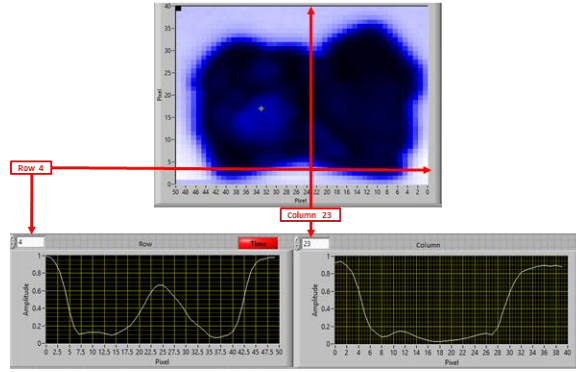


Figure 20. Row and column trend graphs.

The third and final of the image inspection tools offered in this software package is the pixel cursor. The purpose of this inspection device is to allow graphical or numeric selection of an individual pixel within the reconstructed image. If graphically selected, the cursor information box provides the pixel position and numeric value. This allows the user to select a specific location within the image and obtain the location so that the pixel review toolkit can be used to more thoroughly investigate the spectroscopic response. Likewise, if the user desires to locate a specific pixel that is under review, the cursor can be moved numerically to the exact position.

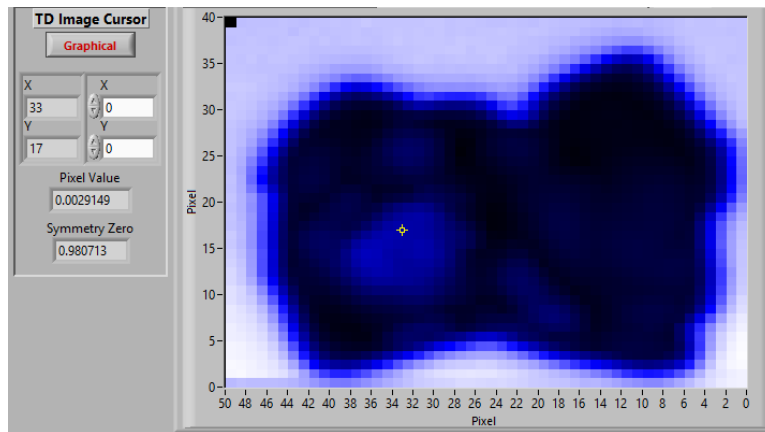


Figure 21. Utilization of the pixel cursor to identify pixel data.

4.3 Image Reconstruction Methods

4.3.1 Basic Time Domain Reconstructions

For all reconstruction types, the desired criteria is selected with a simple case structure and extracted pixel by pixel, using for loops, to directly populate the m-by-n image array. After the array has been fully populated, gain and image interpolation are applied to the array. There are six basic time domain image construction types used by this software. They can be divided into three main categories depending on what type of information they extract from the images.

The first category includes three reconstructions all based on the maximum value of the THz wave intensity. When a *Regular* image is initially loaded, the default time domain image type that appears is the ‘Peak Amplitude’ image. To construct this image, the software extracts the maximum value of the waveform for each pixel’s signal. This type of image tells only the relative intensity of the terahertz as it passes through different areas of the sample. It does not take into account the situation wherein the radiation experiences a phase shift through the sample material sufficient to cause the waveform to invert. This issue is addressed by the second form of amplitude reconstruction referred to as ‘Peak Absolute Amplitude’. In this case, the absolute value of each waveform is taken before the maximum is extracted.

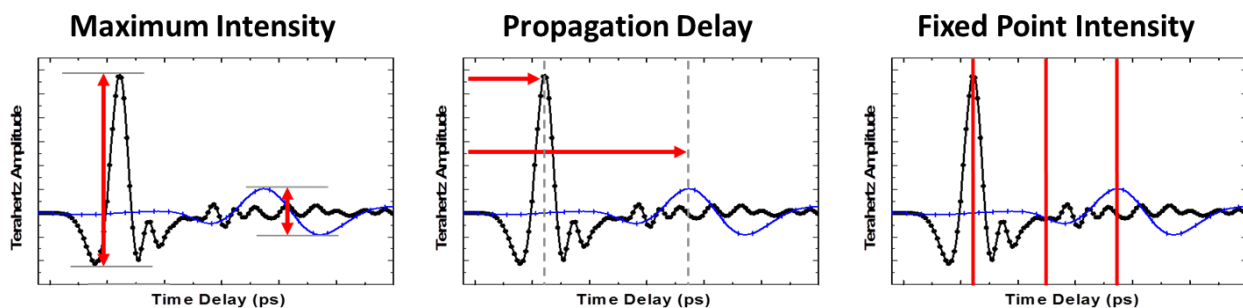


Figure 22. Waveform visualization of reconstruction methods.

Comparing these two can be very useful not only if a section of the material actually inverts the terahertz pulse, but also if the spot of radiation is centered such that a “split peak” occurs. A split peak refers to a spectroscopic scan in which two material types with well separated propagation delay of the peak intensity are within the spot of the radiation. When this occurs, two peaks can appear at the delay times associated with their material type. Because part of the radiation is incident on each section, the two peaks are drastically reduced in intensity. Some of the time, the peak separation can occur such that a point of local minimum for both materials occurs at the same delay time. This can result in a dip between the peaks that is significantly larger in amplitude than the two individual peaks in the spectrum.

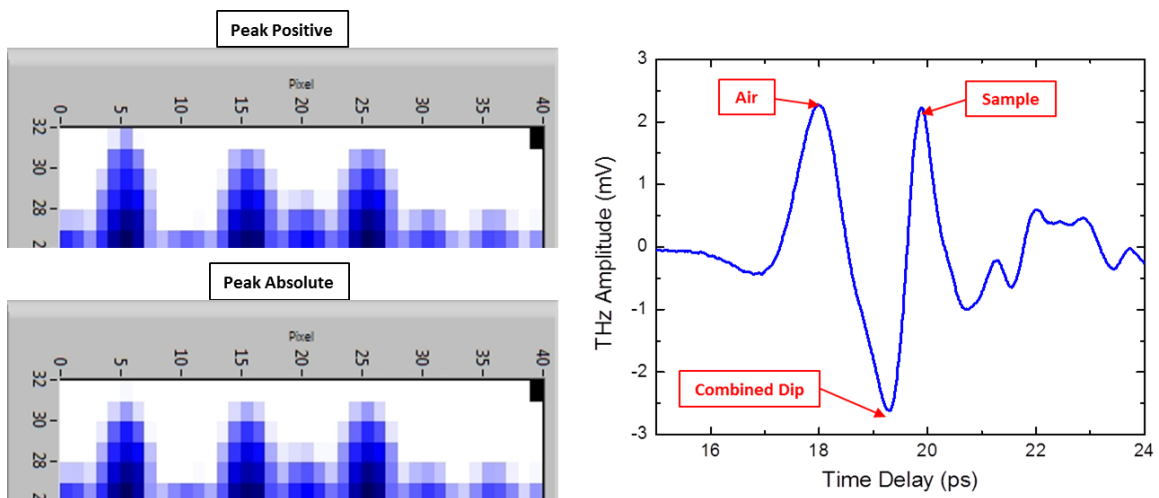


Figure 23. a) Difference in Peak Amplitude and Peak Absolute Amplitude images and b) example of a split pixel spectrum.

Images may also be constructed by taking the difference between minimum and maximum values within the wave. These are referred to as Peak to Trough Amplitude images. This is the third time domain amplitude reconstruction method. One advantage of this type of image is that the split peak pixels can in some cases show completely different behaviors than the non-split pixels around them.

The next two time domain image constructions are based on the relative time-of-flight for the THz radiation. For these the x-axis value time domain waveform that correlates to the peak amplitude of either of the first two methods that have been detailed is used to populate the image. The software determines the index value of the m-by-n array at which the peak intensity occurs, and then constructs an image from the corresponding values from the x-axis vector. The standard contrast method applied gives a higher value to the peak that occurs later in time and a lower value to those that occur earlier. Absolute and positive imaging is available for this type of construction as well. In the case of these split regions, the peak absolute images very sharply show the split regions in an image of the pins on a microchip.

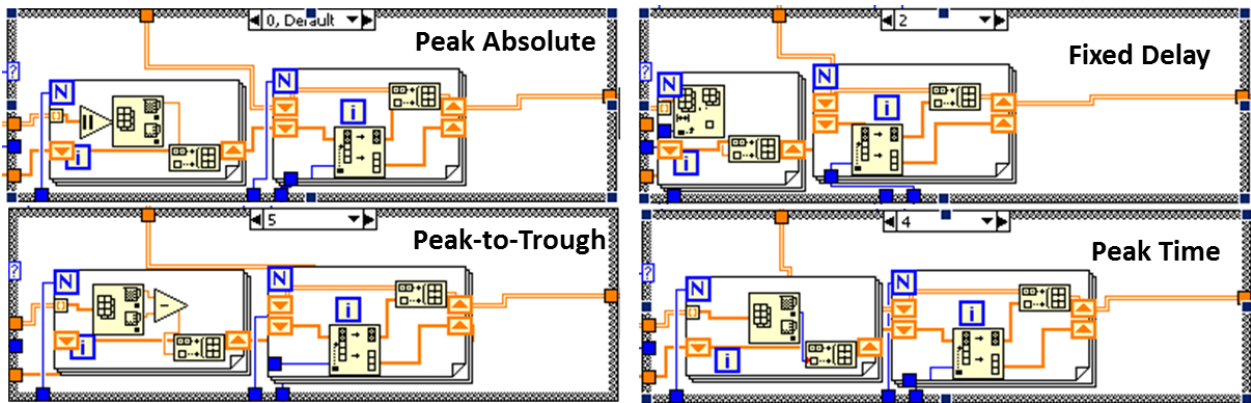


Figure 24. LabVIEW Block Diagram for basic time domain pixel extractions.

The last basic time domain imaging type is fixed delay imaging. In this imaging type, a point within the time window is selected, and the amplitude of all pixels at that point is used to construct the image. This is the only one of the basic time domain imaging types that does not specifically focus on the peak intensity of the terahertz. In effect, this imaging method allows the state of the terahertz wave to be examined simultaneously for every pixel at any point within the recorded time window. There are numerous advantages to looking at data in this way. First, by focusing on the peak time of a specific material type, high contrast can be achieved between

that material and all others within the sample. If the scan window is made large enough, then the amount of time for a material's pulse echo can be determined. The software allows the user to control the delay position with a slider, and as long as rigorous interpolation is not being applied, the updating of the image occurs in real time.

4.3.2 Time Domain Derivative Imaging

Images of the derivative of the time domain signal can also be constructed. There are four types available to use with the toolkit. For these imaging types, the time derivative of every waveform is computed individually using the basic LabVIEW tool for discrete differentiation. The first such image is the image of the derivative positive peak. This image identifies the maximum positive slope that the THz pulse experiences within the scan window which generally corresponds to the sharpness of the leading edge on the main peak. The derivative negative peak can also be used for image reconstruction, with typically represents the sharpness of the tailing edge on the main peak. By contrasting these images, the symmetry of the THz pulse through different material regions can be assessed.

The next derivative image construction method is derivative width. In this method of construction, the spacing between the positive and negative derivative peaks is used for the image. The array indices corresponding to these two values are extracted, and the time difference between them is determined by subtracting and taking the absolute value. Since these two time positions are generally associated with the points of inflection on either side of the main THz peak, this image method is often useful for identifying pulse broadening that occurs as a result of the material interaction.

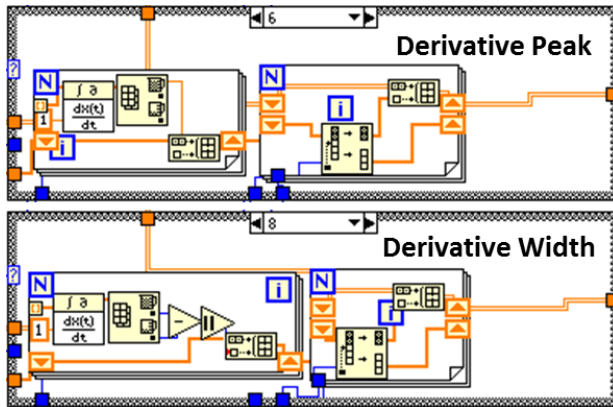


Figure 25. LabVIEW Block Diagram for d/dt pixel extractions.

Finally, fixed delay imaging is also available for the derivative of the time domain signal. In the same ways that the normal fixed delay imaging informs about the intensity, the derivative fixed delay informs about the rate of change of the pulse at a fixed point in time.

4.3.3 Frequency Domain Image Construction

There are six basic frequency reconstruction methods. Images can be constructed for amplitude, phase, or power; and additionally, the frequency domain derivatives of each. In all of these cases, a specific frequency is selected for the reconstruction and the required parameter associated with that frequency is extracted from the spectra.

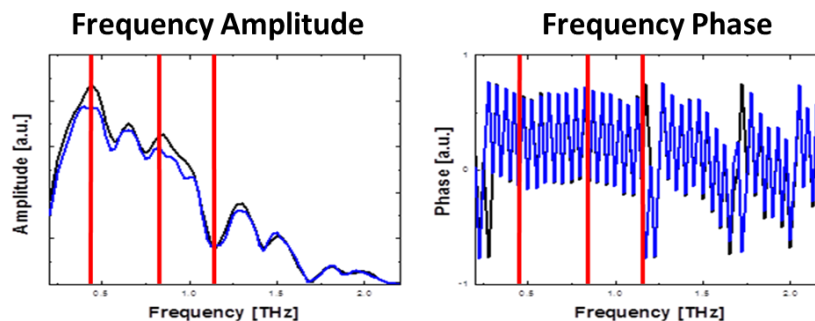


Figure 26. Representation of frequency selection for amplitude and phase spectra.

The first type of frequency image that can be selected is the Frequency Power image. Power is the decibel representation of the transmission spectrum. When observing this type of frequency spectrums that result from terahertz measurements, power spectrum is most notably important when looking for strong absorption features such as water lines. Differences in intensity that do not relate to these types of strong absorption features are easily lost in power spectrum imaging.

To generate the most basically understandable frequency images, the frequency amplitude spectrum is used. Rather than emphasizing only absorption peaks, linear differences in spectrum intensities are more readily examined. Phase imaging is also within the capability of the system. An inherent difficulty in the interpretation of phase image reconstruction results from the 2π ambiguity; that is, phase changes at a given frequency can only be understood to have the represented phase value, plus or minus $2n\pi$ (where n is an integer).

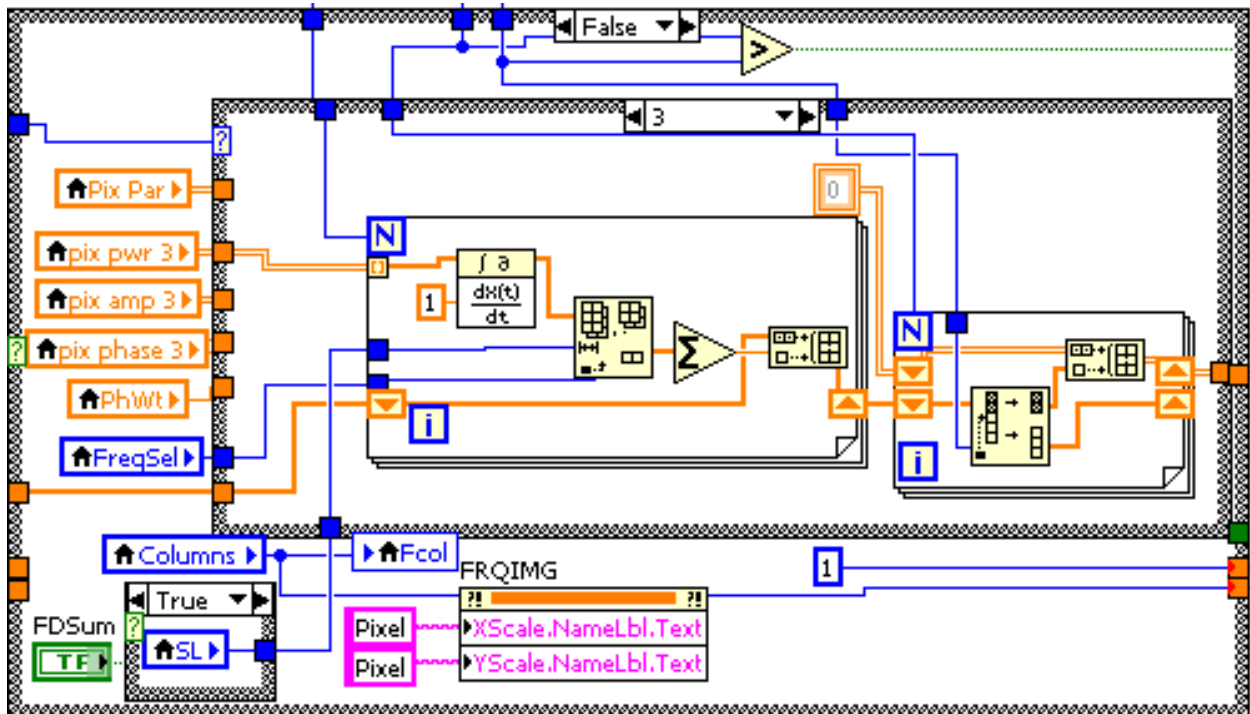


Figure 27. LabVIEW Block Diagram for frequency domain pixel extraction.

In the frequency domain, derivative imaging plays a significantly more important role in the visual interpretation required for image analysis than in the time domain. In comparing power or amplitude spectrums, there are cases where the absorption peak of a spectrum with higher intensity remains at a higher value – or drops in intensity only enough to become approximately equivalent – than the corresponding spectrum for a lower intensity region. Because of this, resolving actual absorption peaks can become extremely difficult if only the three imaging methods already presented are used.

For power derivative imaging, the frequency at which an absorption peak occurs becomes a zero (or arbitrarily close) in the derivative of the spectrum. Similarly, the frequencies immediately before and after a feature have extremely high derivatives. The actual amplitude differences of the spectra have only a minimal influence on the derivative imaging, thus only the features of interest will be strongly visible.

Amplitude derivative imaging presents more similarly in function to the fixed delay derivative time domain imaging. If investigating a material with relatively broad resonance behaviors or frequency ringing, this type of imaging can be effectively implemented to resolve understanding of the frequency behaviors of the sample.

4.3.4 Advanced Image Reconstruction Methods

There are three advanced image reconstruction methods that can be used to provide additional insight into the response of an imaged structure. All three of these are used in conjunction with the image reconstruction techniques detailed in previous sections. They are reference image comparison, multiple parameter imaging, and frequency summation.

Multiple parameter imaging is utilized for the time domain reconstructions. For this, up to three different imaging criteria are selected simultaneously to apply to the final image array. These can include any combination of the basic time domain or time domain derivative image reconstruction parameters. The software sums the weighted average of the three normalized image arrays together, re-normalizes the result, and then applies the user defined gain onto the result. This technique is particularly useful when regions of a sample have close similarity on one of the criteria but are significantly different on another; such as when the amplitude are close to the same, but the propagation delay is significantly different.

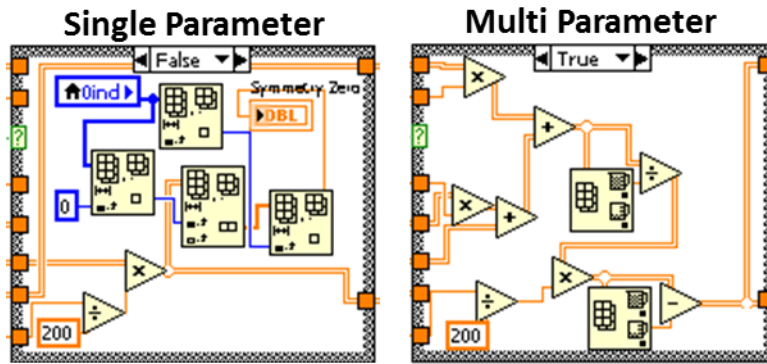


Figure 28. LabVIEW block diagram for single and multiple parameter reconstructions.

The next advanced technique we apply to the frequency domain image – the sum over a discrete range of the spectra. This is useful both for observing overall transmission of radiation over a broad region of the spectrum, as well as sharp identification of comparatively shallow absorption peaks that occur over ranges from 50-200 GHz. A single frequency transmission ratio image would simply be the scalar division of the pixel intensities, and since the same denominator would be used for each division, the same effect can be achieved by applying a lower than unity gain to the image contrast. Thus, by applying a summation over a small region, the behavior of the transmission ratio can be observed clearly. In addition, this method is important in cases where neither the overall amplitude nor the slope exhibit a change that is large

compared to the average value at a single frequency, yet a real absorption effect is present in the transmission behavior of a material.

The final advanced reconstruction technique is reference image comparison. To use this, two images of equal dimensions must be acquired. Both images are loaded simultaneously into the analyzer software independently. The application utility of comparing two images differs slightly in the time and frequency domains. In the time domain the images can either be subtracted or divided pixel-by-pixel, after which any of the time domain reconstruction techniques can be applied. The practical application of this is for ‘before and after’ imaging of a sample that has undergone a quantifiable change, or for substrate subtraction on a semiconductor or metamaterial device structure. In the frequency domain, the reference image is primarily valuable for determining the frequency dependent transmission ratio of an imaged structure. This capability allows for fast and accurate observation of the quality and uniformity of devices designed with frequency specific effects such as meta-material absorbers.

CHAPTER 5: INORGANIC IMAGE RECONSTRUCTION

Biological materials are, in general, highly inhomogeneous and complex structures. This can make interpretation of spectroscopic images difficult; particularly when the spatial resolution of the images is low compared to the size of biomolecules and thickness of tissue layers. Because of this, it is advantageous to begin by imaging a relatively simple, homogeneous inorganic structure. The uncomplicated nature of the sample and relatively large regions of single material type allow for examination of the sensitivity and capability of our image reconstruction techniques with drastically reduced ambiguity.

5.1 Sample Description and Experimental Details

The memory microchip shown in the previous chapter consists of a small integrated circuit (IC), encapsulated in black, opaque plastic. At two points along the surface of the plastic, small circular indentions are visible. These indentions correspond to manufacturing defects due to the plastic molding process, and as such, the material is slightly thinner at this location. Along two edges of the chip protruding metal pins connect from the IC. All but three of these metal connectors were removed to leave only small metal nubs, and the remaining three on one side were bent outward so that they orient normal to the propagation vector of the radiation.

On one surface of the chip the letter 'A' was drawn using silver paint centered over the IC (the letter appears sideways in the images). The conductive silver paint in its liquid form consists of silver and non-metallic bonding agents suspended in an acetone ethanol solution.

When the paint sets, the organic solvents evaporate out of the solution and all that remains is the bonding agents and the conductive silver. Since the paint was applied by hand, the thickness is not entirely uniform. Instead, the paint is slightly thinner in the legs that protrude than at the center triangle.

The chip was measured by the THz-TDS operating in transmission mode. The chip was mounted in the spectrometer such that the incident radiation passed through the object before reaching the paint. Image acquisition was performed for a region 20mm x 16mm with a pixel pitch of 0.5mm. The chip is longer than the maximum window size of the THz-TDS imager, thus only part of the object is visible within the image; however, all of the major features of the sample fit within the window. All pixels consisted of a 6ps long time domain window selected such that the primary THz response of all locations on the microchip would fall within this window. It is noted that to capture the primary peak of the background, which occurs 8ps before the first peak from the sample, the time domain window would have to drastically increase. Since the background is not important for this analysis, the time range was not extended to contain this information as it would drastically increase the image acquisition time from 12 hrs. to 26 hrs.

There are two primary motivations for imaging this specific sample. First, because components of the sample are not apparent in the visual spectrum without opening the casing and THz radiation should penetrate the plastic shell and reveal the contents. Second, the plastic casing itself is of uniform thickness over most of the surface, but at the bonding sites and along the edge the plastic is significantly thicker in the propagation direction, and therefore some contrast should develop as a result of this. The connection pins are largely composed of metal; therefore the expectation is that they should be entirely opaque to THz radiation. Dried silver

paint is primarily metal, thus it should drastically reduce transmission; however, it is an inhomogeneous mixture of metal and the non-metallic bonding agent. Likewise the CMOS chip at the heart of the device is a mixture of sub-wavelength metallic structures on a semiconductor substrate. Due to this some transmission may be observable. Because the metals are simply blocking transmission, they should not introduce a propagation delay on the THz. The plastic non-uniformities and non-metallic components of the silver paint, on the other hand, should reduce the transmitted intensity due to absorption within the material and the THz time-of-flight should be extended as it passes through.

5.2 Results and Discussion

5.2.1 Time Domain Reconstruction

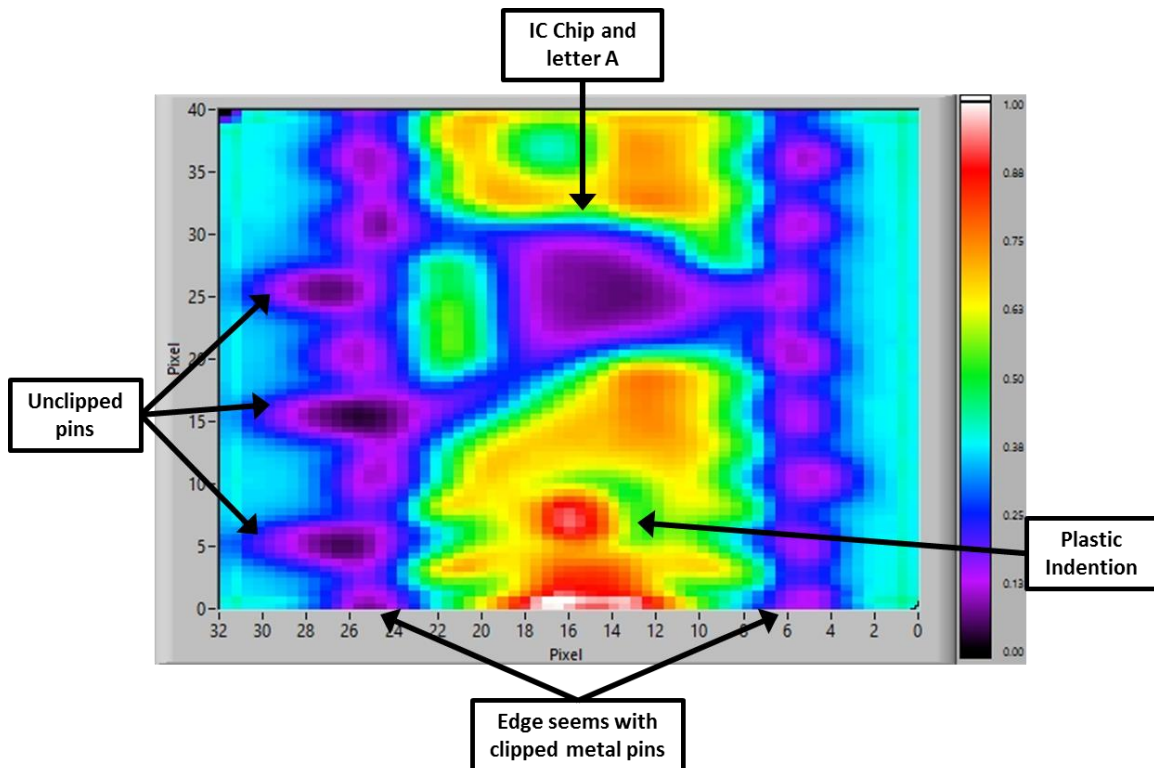


Figure 29. Time domain peak-to-trough image of microchip using color contrast, interpolated bicubically to 4976 pixels.

Observing the peak amplitude image result (Figure 29), the first thing of note is that the transmission is drastically reduced through the regions containing metal. The exact shape of the three protruding metal pins cannot be clearly resolved but the locations of each is recognizable as well as the location of every nub along the edge. In addition, the THz radiation was not completely blocked. This low resolution and lack of complete THz suppression are both a result of the features being smaller than the average spot size of the radiation at the focal plane. The plastic indentation and CMOS chip locations are also clearly in evidence. Where the legs of the letter 'A' extend towards the side of the chip can also be recognized, but the opening in the center of the letter (where only the CMOS chip is in the propagation path) cannot be distinguished from the area containing only the lettering or both chip and silver paint.

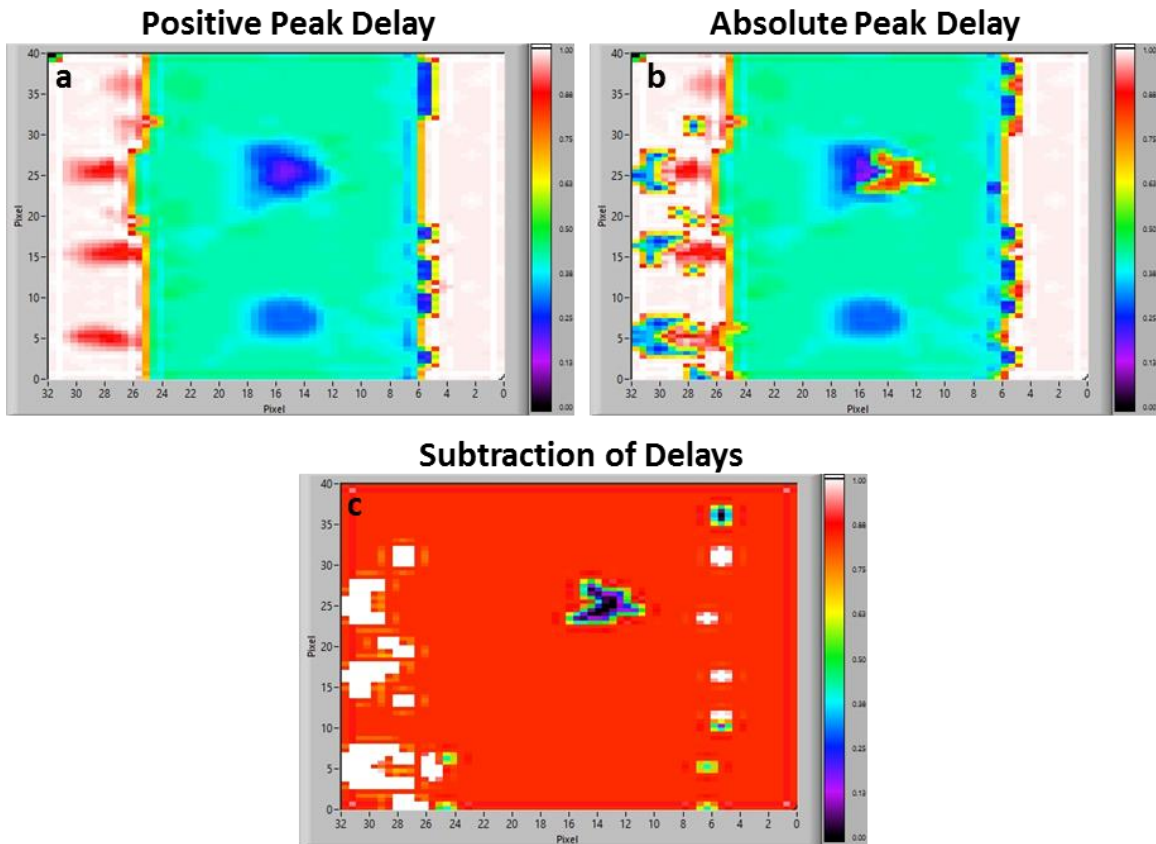


Figure 30. Time domain propagation delay images of microchip using color contrast, interpolated bicubically to 4976 pixels.

The propagation delay (Figure 30a) of the primary peak also does not reveal a significant insight into this distinction, though the center location of the letter and the location of the indentation indicate a faster propagation of the radiation through the material. If we take the absolute value of the spectrum before extracting the delay, however, two features become immediately apparent (Figure 30b). First, the overlap between the top of the ‘A’ and the CMOS chip is clearly visible. From this we know that in this region although the THz intensity is of the same overall amplitude, the peak of the overlap region is phase shifted by 180° and delayed. Another thing that this reconstruction tells us is that at around the edges of the three extended metal pens, the radiation is similarly affected. For both of these regions, a split-peak behavior is occurring; however it split in this case, the split peak regions can be resolved clearly by suppressing the similarities in these two images and only observing the difference (Figure 30c).

5.2.2 Frequency Domain Reconstruction

For the frequency domain interpretations, we expect a general trend where materials with a stronger THz absorption decrease the transmitted THz amplitude to the noise threshold more rapidly as the frequency increases. To show this trend, four frequencies have been selected for reconstruction (Figure 31). At 0.45 THz, the transmission through the extruding pins and the CMOS IC are already less than 2% of the normalized maximum observed intensity. As the frequency increases above 0.6 THz, clear contrast between the body of the microchip and the indentation becomes clearly definable. This is a broadband difference, however, as opposed to being attributable to specific absorption frequency. Above 1.5 THz, all contrasts within the chip except for the single point where the plastic is thinner disappear. From this, it is concluded that the frequency transmission amplitude cannot resolve any contrast in the overlap region between

the silver paint and the IC, and is therefore insufficient to fully resolve every aspect of this object.

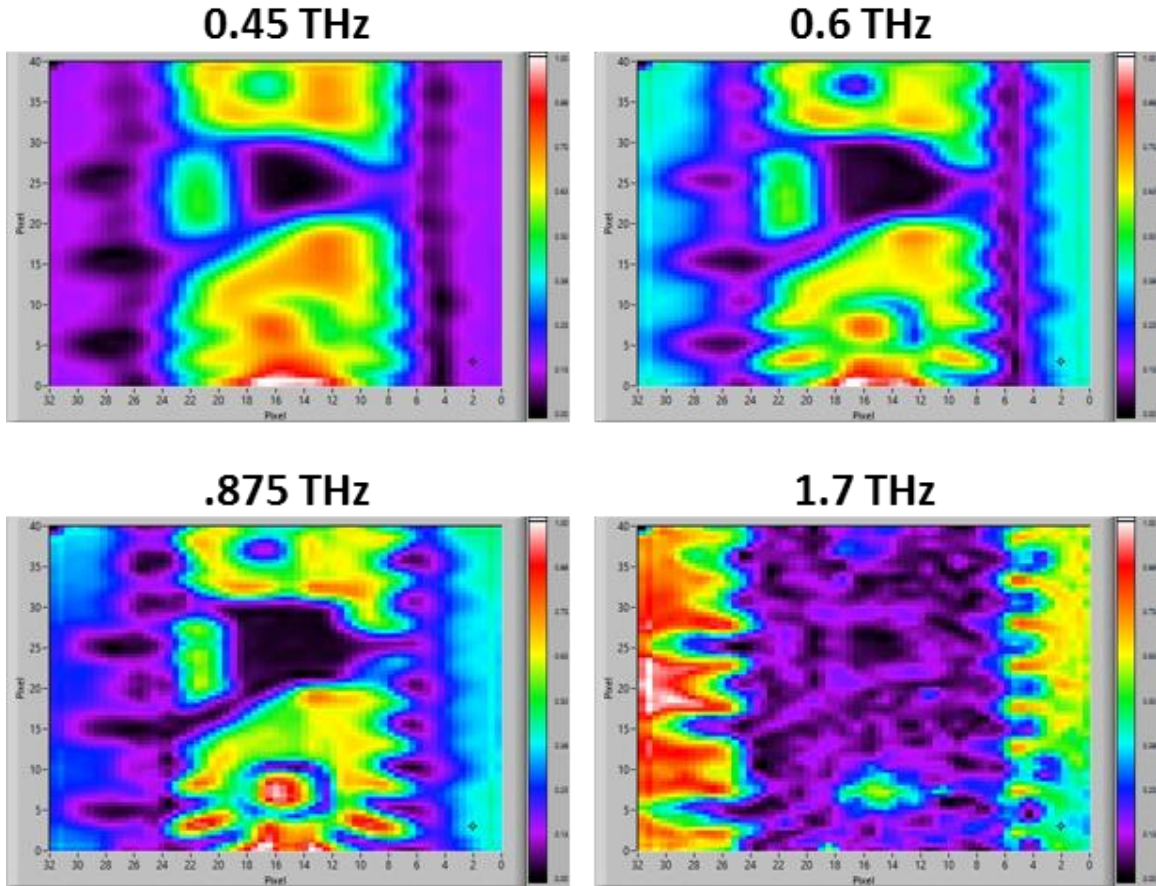


Figure 31. Amplitude reconstructions at select frequencies of the microchip using color contrast, interpolated bicubically to 4976 pixels.

Phase reconstruction proves to be more beneficial for identifying this region of the sample (Figure 32). Observing low-frequency reconstruction (again at 0.45 THz) a strong shift occurs both at the overlap region and around the edge of the metal contacts. This agrees with the inference made from the propagation delay reconstructions; however, it identifies that this clearly defined propagation shift primarily affects the longer wavelengths. At frequencies above 1 THz, these regions are no longer sufficiently out of phase to provide reliable identification. There is also another important insight that these reconstructions provide; in the region between

1 THz and 1.5 THz, the radiation is out of phase only in areas that present a distinct topographical change in the direction of propagation. What I mean by this is anywhere that scattering can occur due to the surface of the sample being non-normal. This includes the outline of the microchip itself, the lip of the plastic indentation, and the contours in the silver paint.

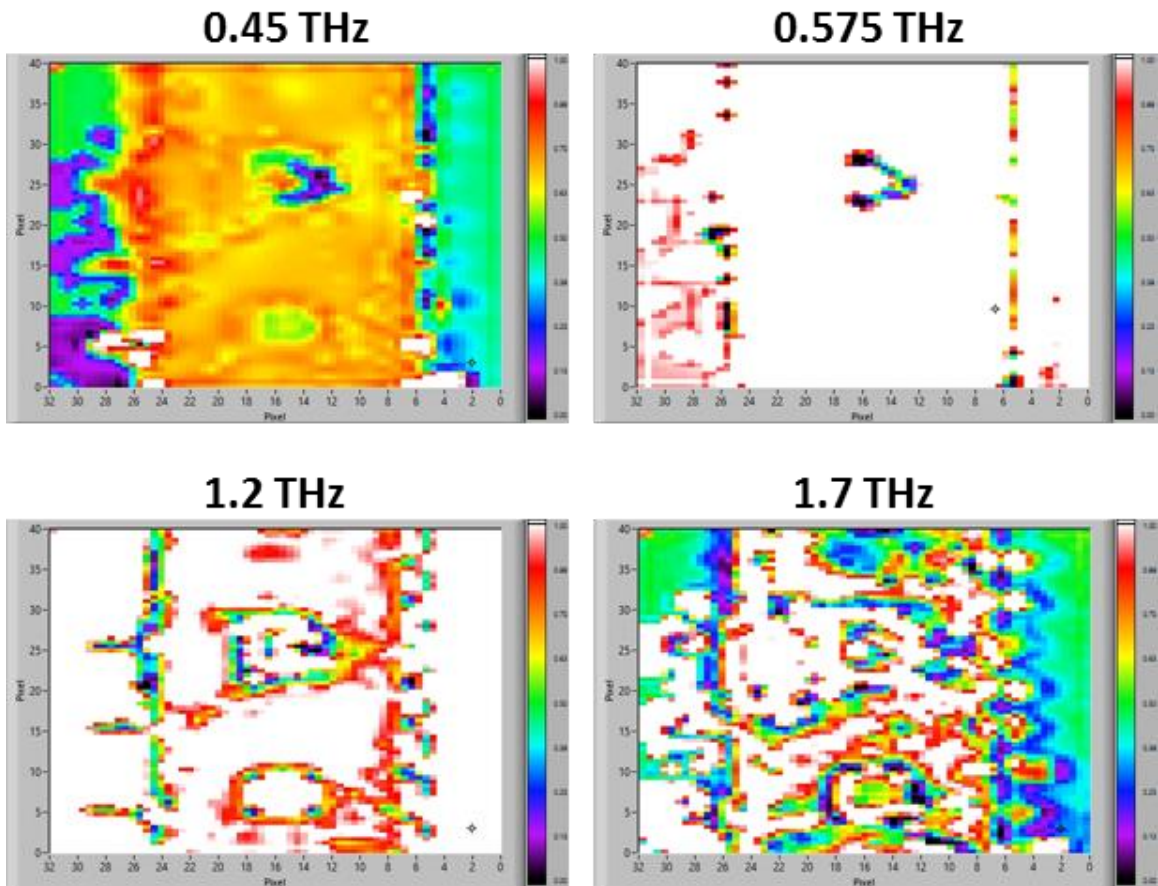


Figure 32. Phase reconstructions at select frequencies of the microchip using color contrast, interpolated bicubically to 4976 pixels.

CHAPTER 6: IMAGING OF BIOLOGICAL SAMPLES

6.1 Osseous Tissue Identification

6.1.1 Sample Preparation and Experimental Parameters

The first biological study in which the image analysis techniques presented in the preceding chapters were fully exploited was in the identification of osseous tissue types. For this work, a thin cross-section was taken from the distal epiphysis of a chicken femur (Figure 33a). The sample was selected because several of the osseous tissue types could be visually distinguished, which allowed for the identification techniques to be easily assessed. To prepare the bone, a large piece was histologically fixed using a 10% formalin neutral buffer and then a 2mm thick slice was taken for imaging. This process provides several services that are useful for our purposes. First it crosslinks the protein chains so that the structural integrity of the sample remains intact. This additionally prevents any further mortification of the tissue during measurements. It also dehydrates the tissue which is of particular importance for THz applications since water is an extremely strong absorber.

Once the sample had fully dried, it was mounted in the spectrometer by clamping it firmly between two thin polypropylene sheets. Polypropylene was selected because it is an optically transparent material that results in less than 10% intensity reduction of the propagated THz radiation. Due to the methodology of the THz-TDS that is used here, this image required 27 hours to complete. If the sample were active (living) biological tissue, the imaging time would potentially prevent the system from capturing an accurate image; however the formalin fixing process and atmosphere control were sufficient to negate this issue. This was verified by

performing a spectroscopic scan on one location of the tissue before and after imaging – where no difference in spectrum was observed.

The image acquisition was performed over a region of 20 mm x 16 mm, which captured the entire sample. For this image, a pixel pitch of 0.4mm was used in both directions with a final pixel count of 2000. The THz-TDS waveform over a region of 16ps was acquired for each pixel with the scan start position set 3ps before the primary peak that was observed through the polypropylene sheets alone. Although increasing the time domain scan length drastically increased the acquisition time, it was necessary in the case of this sample. For some of the tissue types of the sample, significant propagation delay was observed; for other regions, the radiation is not strongly delayed from the background region. In this case, if a shorter time scale were selected, the incomplete time-domain waveforms would result in image reconstructions that did not accurately reflect the nature of the sample.

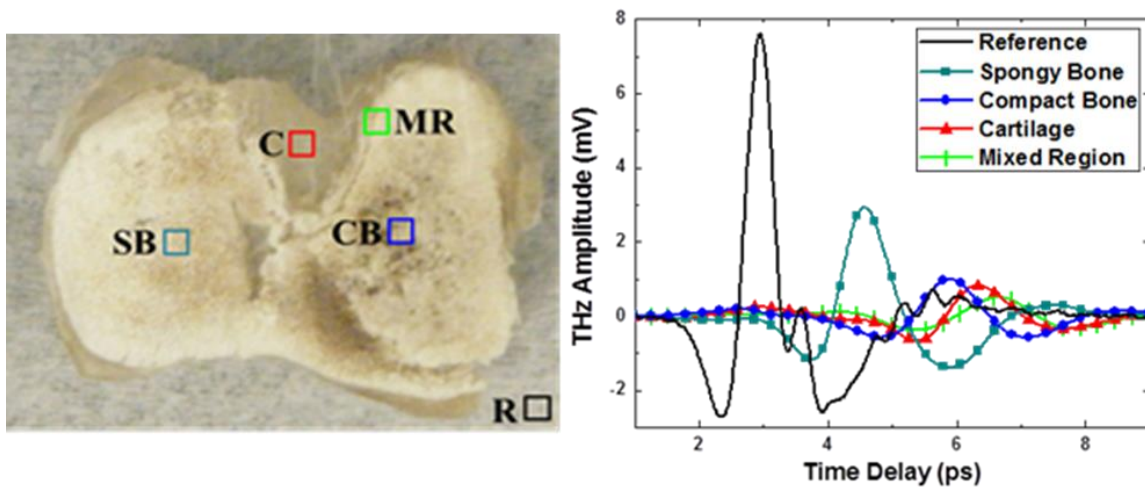


Figure 33. a) Picture of chicken femur cross-section with locations of each baseline scan indicated, and b) THz TDS results for each baseline.

Time Domain Peak Intensity			Propagation Delay		
	mV	unity gain	230% gain	Delay ps	unity gain
Reference	7.60	1.00	2.33	2.8	0.43
Spongy Bone	2.93	0.39	0.90	4.42	0.68
Compact Bone	1.00	0.13	0.31	5.73	0.88
Cartilage	0.82	0.11	0.25	6.18	0.95
Mixed Region	0.50	0.07	0.15	6.53	1.00

Four primary tissue regions were identified in the sample based on the known anatomical composition: spongy bone, compact bone, cartilage, and the mixed region comprised of both compact bone and cartilage. Individual spectroscopic scans were obtained for each of these characteristic regions. Since this sample is a complex organic structure, the main motivation in this sample selection is to assess the validity of the assumption that single point, baseline scans can be used to select characteristic responses of each tissue type for image reconstruction. Thus we will select all of the reconstruction criteria from inspection of these spectra, and compare the quality of the image results for distinct representations.

6.1.2 Time Domain Analysis

The time domain results are shown in Figure 34b. From these baseline waveforms, we observe that the spongy bone transmitted much more strongly than the other tissue types (peak amplitude of 2.9mV), which makes sense due to the relatively high porosity of this tissue. This is approximately 40% of the reference signal; and therefore contrast for this tissue should be easily obtainable. Contrast among the three remaining tissue regions, on the other hand, will be more difficult to develop. These regions, the compact bone, connective tissue (cartilage), and

selected mixed composition region all exhibited peak amplitudes between 0.5 and 1.0 mV. The transmission through cartilage is slightly lower than that of the compact bone, and this may indicate that the formalin fixed cartilage has a higher structural density than the fixed bone.

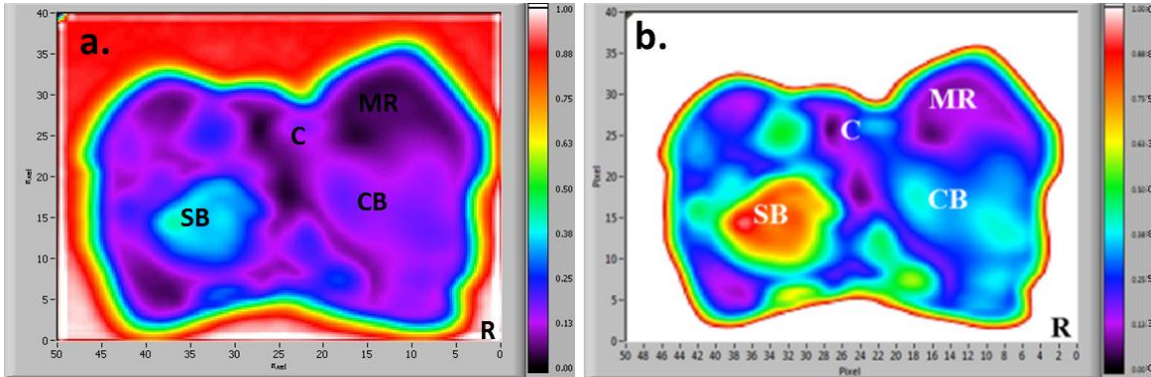


Figure 34. Time domain Peak intensity image reconstructions using color contrast for a) unity gain and b) 230% gain.

Indeed, based on the initial time domain peak reconstructions alone, the compact bone, cartilage, and mixed region do not develop significant contrast; however, if we adjust the gain scale such that the spongy bone exhibits 90% on the intensity scale, three of the four regions become identifiable. It should be noted that some regions do not appear uniform even over areas much larger than the THz spot-size. The phenomenon is expected for the mixed regions since the composition ratio of tissues is not constant. This loss of definition is particularly pronounced in the area of the sample containing only connective tissue, but it is easily understood when the inhomogeneity of the cartilage structure and density inherent to the tissue is taken into account.

When the propagation delay is rendered for the tissue sample, it is clearly observable that each type of tissue exhibits an inherent time-of-flight for the main THz pulse (Figure 35a). Compared to the arrival time of the reference pulse, the spongy bone delays the radiation 1.6 ps. The other three delay from the reference by: 2.9ps for compact bone, 3.4ps for cartilage, and 3.8ps for the selected mixed region. Since these three peaks are still closely packed, we observe

only slight contrast. A more critical inspection of the baseline reveals that the minimum value of the cartilage waveform is of a slightly higher magnitude than the positive peak intensity and that it occurs earlier than the maximum observed for the compact bone. Due to this, by taking the time-of-flight for the absolute highest magnitude, as in Figure 35b, the cartilage distinctly contrasts. To understand this behavior more accurately, we must investigate the frequency response.

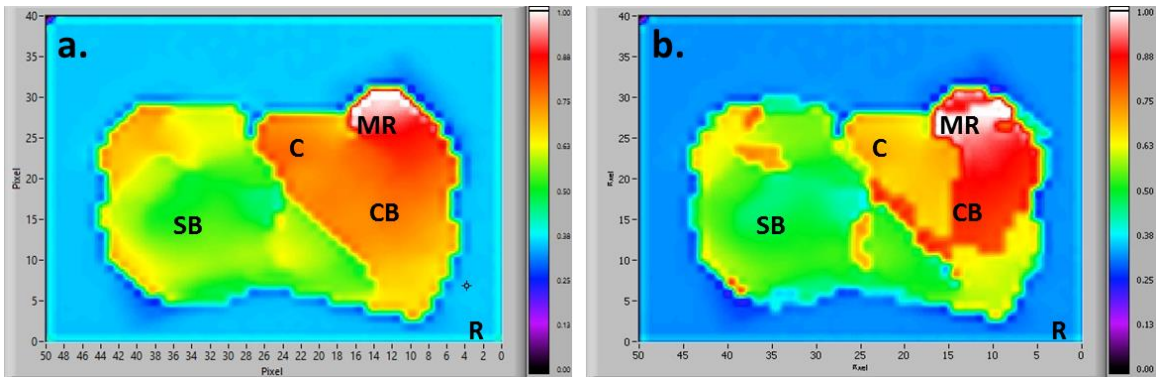


Figure 35. Time domain propagation delay image reconstructions using color contrast for a) positive peak and b) peak of the absolute value.

Before moving to the frequency domain, there are several other time domain reconstruction techniques that can provide both verification of the methods and further insight into the behaviorally response of the interaction. The first is fixed delay imaging. This method of image reconstruction is only practical if characteristic reference scans have been taken and properly analyzed. By observing the relative time evolution of the different baseline responses, points within the time window can be strategically selected to highlight the specific responses associated with a single tissue type. In addition, if the behavior of the material is understood, future samples can be tested for their presence utilizing the *Fast* scan experimental method, which will reduce imaging time.

In Figure 36, three fixed positions within the time domain window have been selected. The first is the most natural selection: the one corresponding to the spongy bone peak. All other baseline spectra have extremely low amplitude at this position, so only the desired tissue type exhibits a strong THz response. The next image centers on the peak of the compact bone, where the spongy bone is at a minimum in its intensity and all other regions are washed out. Finally, the third illustrates the peak associated with the cartilage region. From these results, it appears that it is difficult to isolate the cartilage from the other tissue types using a fixed delay at the baseline's maximum. Although all of these techniques can assist in the identification, none of these methods grant a completely clear picture of the sample in a single image.

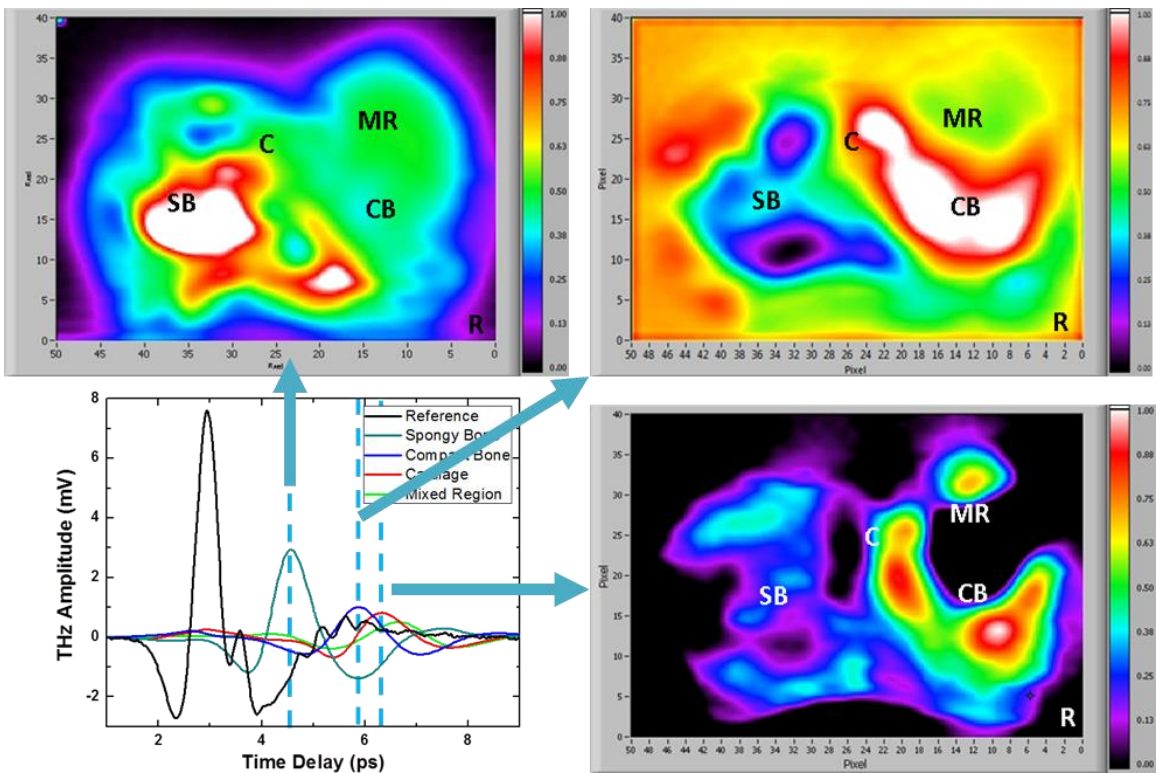


Figure 36. Time domain fixed delay image reconstructions using color contrast.

6.1.3 Frequency Domain Analysis

Figure 37 shows the FFT power spectrum results for the baseline spectroscopic scans used to determine the frequency image reconstructions. As we expect from the time domain, a significant separation exists in overall power between the spongy bone and the other tissue types. From these spectra, we see that the signal through all tissue types falls to the noise floor at 1.6 THz. In addition, distinctions between the compact bone, cartilage, and mixed region become difficult to clearly assess above 1.3 THz. For this reason, we will confine frequency reconstructions to the lower frequencies.

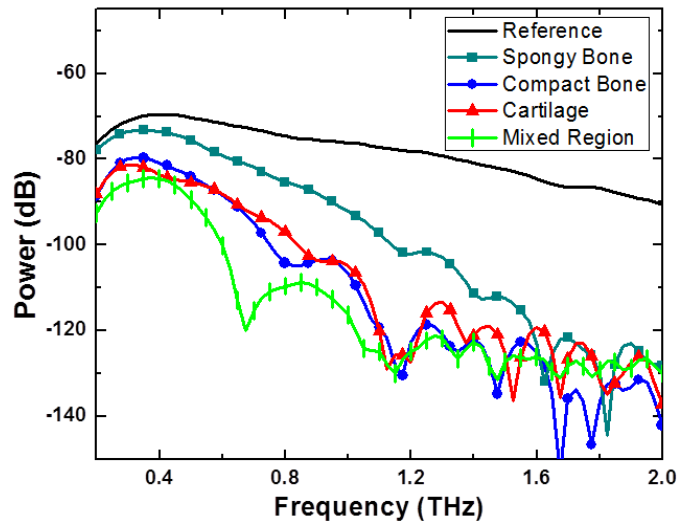


Figure 37. Frequency power spectrum for characteristic tissue baselines.

Over the considered frequency range, the compact bone and cartilage baselines track together very closely, with exceptions between 0.4-0.5 THz, and 0.725-0.875 THz. The mixed region baseline is lower in transmitted power throughout the spectrum, with the cartilage baseline exhibiting an absorption peak between 0.4-0.5 THz that closely approaches the mixed tissue power.

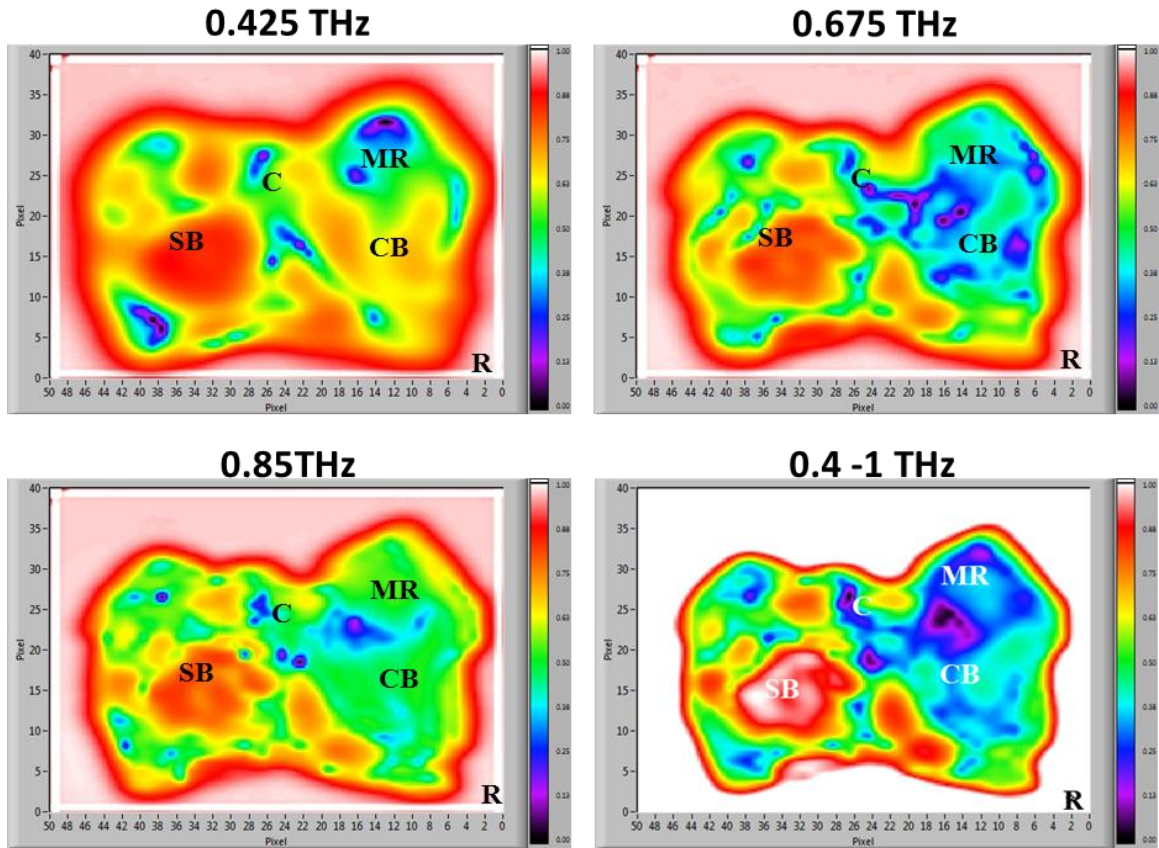


Figure 38. Frequency domain power spectrum image reconstructions at select frequency and integrated over the range using color contrast.

From this interpretation, we thus select the first reconstruction at 0.425 THz (Figure 38a). This reconstruction clearly shows several of the contrasts that we expect. The spongy bone is clearly defined against the rest of the tissues, with a much higher intensity than the rest of the bone. In addition, the region of compact bone does exhibit a higher transmission, with the cartilage and mixed regions developing inhomogeneous contrasts over the same intensity range. The inhomogeneity of the connective tissue is once again clearly in evidence for both of these tissue regions. At a slightly higher frequency, 0.675 THz, contrasts between the three closely transmitting regions are unclear. We also note that the compact bone at these frequencies transmits unevenly as well. This leads to the inference that variations in the compact bone structure, though they do not affect transmission at low intensities, make distinct identification at

these frequency ranges unclear. If further analysis of the compact bone is performed, perhaps the physical interpretation of these variations in transmitted power can be uniquely attributed and thus these frequencies would be of extreme value in diagnostics of the compact bone in cases where no other tissue types are present.

The final single frequency reconstruction used for this sample is at 0.85 THz. This frequency corresponds to the dip observed in the compact bone reference spectrum, and thus we expect the amplitude of this tissue to develop a lower intensity than the cartilage but remain at a higher intensity than the mixed region. In this image, we do observe much higher uniformity of the compact bone than at 0.675 THz; however it is difficult to distinguish it clearly from either cartilage or composite tissue. We also note that when integrating over the frequency range 0.4-1.0 THz, the confusion among the low transmission tissue still cannot be resolved.

From these images, we can conclude that the supposition of baseline spectra selected for these reconstructions do not sufficiently represent intensity or amplitude based reconstructions in either the time or frequency domain. We should note, however, that by using these baselines, the propagation time reconstructions do prove valid for this method. This may suggest that the primary limitation here is insufficient source/transmission intensity of the broadband THz radiation that limits the ability to effectively utilize the higher frequencies for identification.

6.2 Observation of Structural Damage in Cartilage Tissue

6.2.1 Sample Preparation and Experimental Parameters

With a basic understanding of tissue responses and the ability to investigate sample behavior effectively through single pixel spectroscopic analysis in hand, the next step that was taken with this work was to begin investigating changes in biological tissue. For this purpose, we begin by identifying a localized structural change within a tissue sample. To induce this structural change, Hydrofluoric Acid (HF) was selected. HF is an extremely caustic acid to biological tissue in general, specifically to osseous tissues. Under direct exposure to HF, the primary cause of damage is the removal of calcium from the tissue at the exposure site, referred to as acute hypocalcaemia. Thus this exposure results in a significant structural change that we propose to observe in the THz transmission response.

The first tissue sample that was processed for this phase of the experiment was a pure cartilage sample (Figure 39). A single tissue type was selected for reduced complexity of the image analysis. Cartilage was selected specifically due to the fact that it has the lowest calcium concentration of the osseous tissues studied here and thus the structural change due to the HF burn will be less pronounced.



Figure 39. Cartilage burned in two locations by 48% and 24% HF.

To prepare the sample, two locations on the cartilage were exposed to the acid. Each location received a different concentration of HF so that any contrast between the severities of damage resulting from the exposure could be identified and used to re-enforce any associated observational trends. The first burn location received exposure to a 48% aqueous HF solution. The second location was exposed to half the concentration (24%) of aqueous HF. The acid exposure was performed by applying a single drop of solution to the sample surface and allowing the reaction to occur for 60 seconds. At the end of 60 seconds, the tissue was immediately rinsed with DI water to remove the remaining acid, prevent the spread of exposure and halt the reaction. The exposure resulted in a slight discoloration of the tissue; making burn sites are clearly visible as seen in Figure 39. The weight and thickness of the sample were taken both before and after exposure. In both cases the changes in these characteristics were not appreciable when compared to the variance observed among other samples due to the changes in hydration and temperature experienced during the preparation process.

After exposure, the sample was placed in a 10% formalin neutral buffer for 2 hours before being dried with compressed nitrogen. The discoloration from the acid exposure

remained visible after fixing. As with the initial bone sample, the cartilage was mounted between polypropylene sheets and placed in the spectrometer to image. For this sample, an image was obtained over an area of 20 mm x 14 mm with a pixel pitch in both directions of 0.5 mm. A time domain window of ~18 ps was chosen to ensure that the appropriate frequency behavior was captured, and the entire image took approximately 16 hours to complete.

6.2.2 Image Analysis and Discussion

Figure 40 (below) represents the two initial time domain reconstructions that were performed for this sample. In the time domain peak amplitude image (Figure 40a), the locations of both burn sites are easily identified by the increase in transmitted THz intensity relative to the unburned tissue. By extracting and comparing the waveforms of individual pixels (Figure 40c), the burned tissue allows between 18% and 20% of the THz to pass through. Compared to the undamaged tissue, which ranges from 9.6% to 10% transmission, this indicates that the structural damage incurred by the HF exposure destroys components of the tissue structure that are significantly responsible for the absorption (or reflection) of THz radiation.

This inference is further supported by the reduction in propagation delay observed at both burn sites (Figure 40b). The radiation passing through the 24% HF burn is delayed 21% less than if it had passed through unburned tissue. For the higher concentration of acid, 48% HF, this is further reduced by 9%. Though only a small difference in transmitted intensity exists between the two burn sites, the difference in propagation delay clearly distinguishes the two.

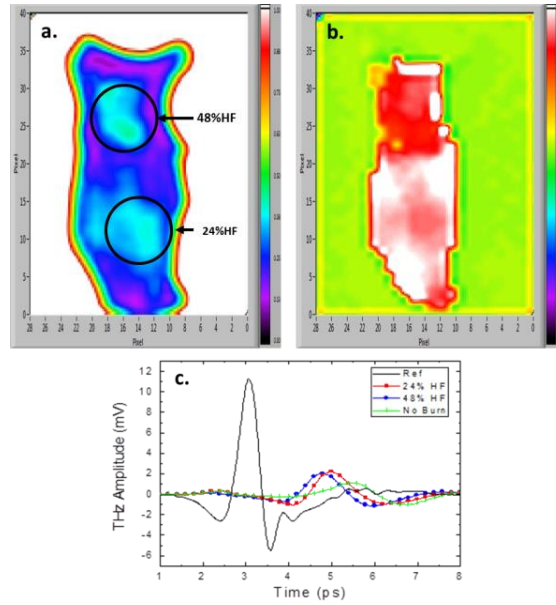


Figure 40. a) TD Amplitude Image, b) propagation delay image, and c) selected TD waveforms from the image data.

The FFT was performed for all pixels with the 18ps window zero padded to 40 ps to allow for appropriate frequency resolution. Figure 41 depicts the images that were constructed from the power spectrum data at 0.45THz and 0.7 THz. The selection of these frequencies for reconstruction was done by first observing the power spectra associated with the pixels extracted in the time domain (Fig. 41c). Next, the image constructions were scanned through the frequency range to ensure agreement between the behavior predicted from the three selected pixels and that observed for the overall image. Above 0.85 THz, a reliable prediction was not possible due to low transmitted intensity of power relative to the noise threshold of the spectrometer. At low frequencies (below 0.6 THz) the burned tissue is clearly contrasted with the undamaged tissue, although, the two burned regions appear approximately the same and no distinction can be made between them. For the intermediate frequency range between 0.6 THz and 0.8 THz, the 48% HF solution has clearly increased the transparency of the tissue; suggesting that more damage to the tissue when compared to the region burned with a lower concentration of acid.

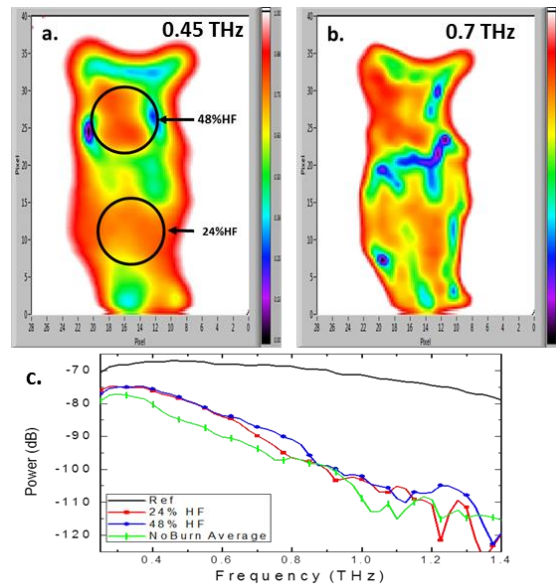


Figure 41. Power spectrum images at two frequencies a) 0.45 THz, b) 0.7 THz and c) frequency power spectra for the selected.

From this sample, the HF burns can be clearly identified in both time and frequency image constructions. Based on these results, the 48% HF solution was selected for further use. Although the higher concentration provides a stronger contrast in transmitted intensity in the 0.6 THz – 0.8 THz frequency range, the more important factor is the propagation delay. For 24% HF solution, the reduction of propagation delay at the burn site is approximately 20% which would place the time domain peak of burned cartilage very close to that of compact bone. By selecting the higher concentration solution for use, the time domain peaks will be distinctly separated.

6.3 Comparison of Structural Damage on Fixed vs. Un-fixed Tissue

The objective of the work presented in this section is to observe and quantify the effects that formalin fixing the tissue on the THz imaging results. We selected a formalin fixative for this (both in the samples here and for the previous two samples in this chapter) because it is one

of the most widely used and accepted histological preservation techniques for organs and tissue. However, the fixation process introduces a large number of new covalent bonds within the tissue that cross-link the primary amino groups of proteins to other proteins and DNA strands. This drastic increase in molecular bonds has garnered specific concerns that THz imaging may provide drastically reduced information about fixed tissue. Studies have been performed, and show that this concern is not entirely baseless; however, the process does not render THz imaging entirely un-usable [93].

There are several differences between the THz-TDS used in this work and that used for the study by Sun and Pickwell-MacPherson. Firstly, the TPI Imaga 1000TM from that study was configured in a reflection geometry; that is, the detector was aligned to detect the THz which reflected from the sample. Second, the study reports only on the changes in the frequency dependent index of refraction and absorption coefficient. As we are neither focusing on material parameter extraction in this work nor operating the spectrometer in reflection mode, it is required that we observe the raw response in the time and frequency domain responses to the histological process.

Two samples are presented for study in this section. Both samples include a combination of compact bone and cartilage, and a single site has been selected on each to which HF exposure has been applied.

6.3.1 HF Burn on Formalin Fixed Osseous Tissue

We begin by preparing a sample in the standard way used for the previously presented samples, first exposing the tissue to 48% aqueous HF for 60 seconds and rinsing with DI water. Next the sample was submerged in the 10% Formalin NB for 2 hours before being dried with

compressed nitrogen and mounted between the PP sheets. This sample, pictured in Figure 42, consisted of clearly delineated cartilage and bone regions such that there are no areas of mixed composition. The white portion on the upper end of the sample represents the cartilage tissue, while the darker section below indicates the compact bone. The HF burn site is located such that both tissue types have been exposed and is indicated in the figure. As with the previous sample, the exposure resulted in a slight green discoloration of the tissue. Unlike the previous sample, however, the burn site is more diffused.

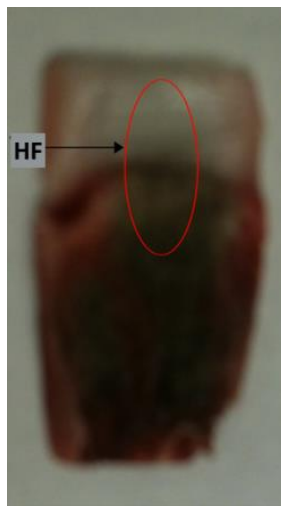


Figure 42. Formalin Fixed tissue with HF burn.

For this sample, an image of 20mm x 20mm was obtained with a pixel pitch of 0.5 mm. A time domain window of 18.6 ps was chosen for each pixel and the image capture took approximately 22 hours. The two basic time domain reconstructions – Peak amplitude and propagation delay – are presented below (Figure 43).

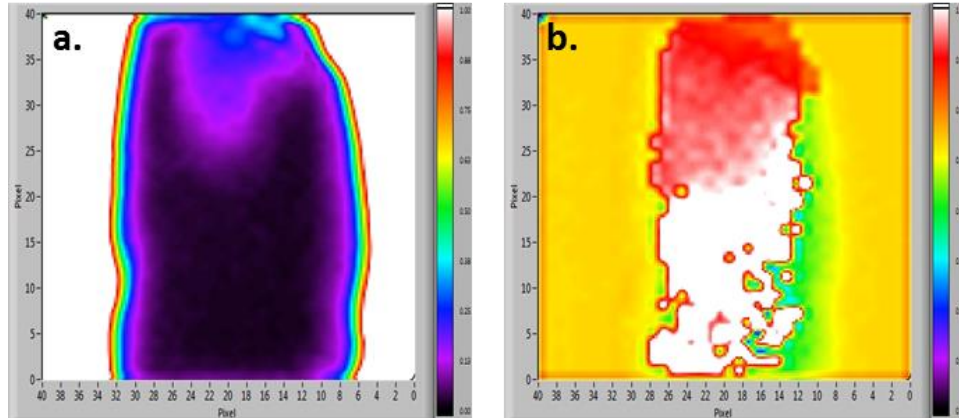


Figure 43. Time-domain images construction from a) peak and b) propagation delay.

From these images, the burn site is distinguishable in the top center of the sample. There is less contrast developed in this sample when compared to the samples presented in the previous section. The maximum time domain intensity passed through the sample is 11% of the reference signal for HF burned cartilage (when compared to the 20% intensity from Section 5.2). This is due to the fact that the sample is slightly thicker. The spectral information for each region of interest is presented in Figure 44. From this data, we see that the expected trend – reduced propagation delay and increased transmission – occurs for both tissue types as a result of the HF exposure. The transmitted intensity through the cartilage increases by a factor of ~ 1.5 , and doubles through the bone region. Similarly, the propagation delay reduces by an average 0.5ps for the bone and 0.8ps for the cartilage. Compared to the effects of the 48% HF burn on the pure cartilage sample in section 5.2, we observe a light decrease in the relative numbers which suggests that full penetration of the tissue with the HF was not achieved in this case. We also observe from this that the HF exposure induces a higher relative transparency in the bone tissue than the cartilage, but does not affect the propagation delay as significantly. This observation agrees with our expectation that the acid would damage bone more severely due to the higher calcium concentration of the tissue.

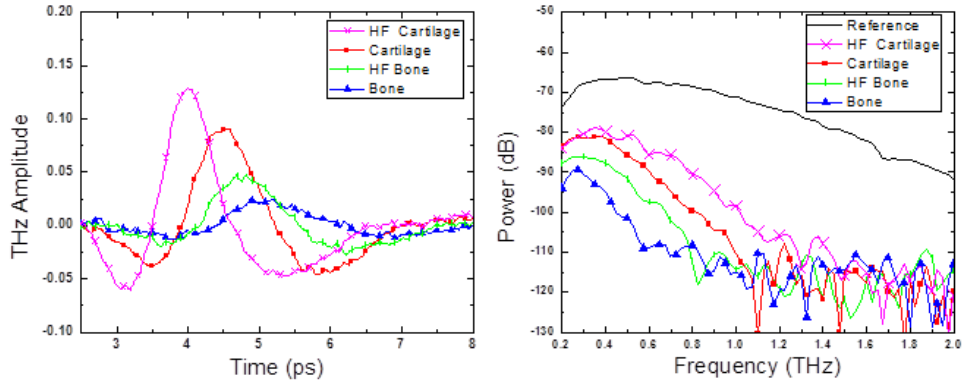


Figure 44. Selected pixel data for a) Time domain b) Frequency Domain from the formalin fixed tissue.

Analysis of the frequency spectra reveals that the bone tissue (both burned and unburned) falls below the noise threshold for frequencies above 0.8 THz. For lower frequencies however, a strong separation in transmitted power is observed; reinforcing the observations from the time domain data. The cartilage tissue exhibits smaller separation at frequencies below 0.6 THz, however the distinction between burned and unburned tissue extends to 1.0 THz before approaching the noise threshold. In addition, the burned cartilage actually exhibits an increase of nearly 0.2 THz in the maximum observable frequency. Reconstructions at 0.45 THz and 0.8 THz were selected to confirm the conclusions drawn from the individual spectra, shown in Figure 45.

As was mentioned in the introductory chapters, excepting for specific absorption lines, higher frequency THz radiation exhibits lower penetration depth. Since the propagation delay of the bone tissue is larger than cartilage we expect a lower cutoff frequency, and due to the smaller change in propagation delay induced by the burn, we also expect less separation in the cutoff frequencies.

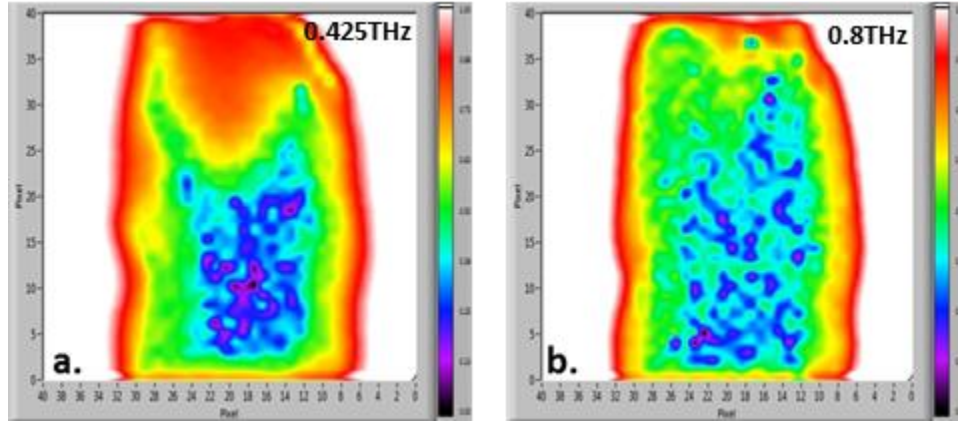


Figure 45. Frequency-domain images construction of power spectrum at a) 0.425 THz and b) 0.8 THz.

6.3.2 HF Burn on Un-Fixed Osseous Tissue

The last step in this study was to observe the THz response for structurally damaged tissue which had not undergone the histological fixation process. Since the acid used to burn the sample induces a structural change in the tissue, and the protein crosslinking incurred during formalin fixation is also a structural change, it is important to observe and understand the interplay between these two processes. For this purpose, a tissue sample composed of both compact bone and cartilage was exposed to 48% aqueous HF and imaged without applying any fixative.

As stated before, the formalin used for previous samples preserves the tissue from decay and allowing the sample to remain intact both during and in between measurements (which can take more than 24 hrs.). Since this sample did not receive the histological treatment, the possibility of decay must be considered. To ensure that this factor did not skew the imaging results, three images were taken over the course of a week and to verify that the THz response of the sample was not significantly impacted during the measurements.

The sample is shown below (Figure 46). Again, the dark region in the lower corner of the sample represents compact bone tissue while the lighter red tissue is cartilage. Two of the images taken of this sample are presented here, the first without exposure to HF and the second after the exposure. The first step to prepare the sample was to dehydrate the tissue using compressed nitrogen. This procedure provided two benefits to the imaging process. Water molecules accelerate the breakdown of collagen and mineral bonds, thus a dry sample decays more slowly. The second reason, as mentioned before, is that even small concentrations of water in the THz propagation path strongly absorb the radiation thereby drastically reducing the signal strength.

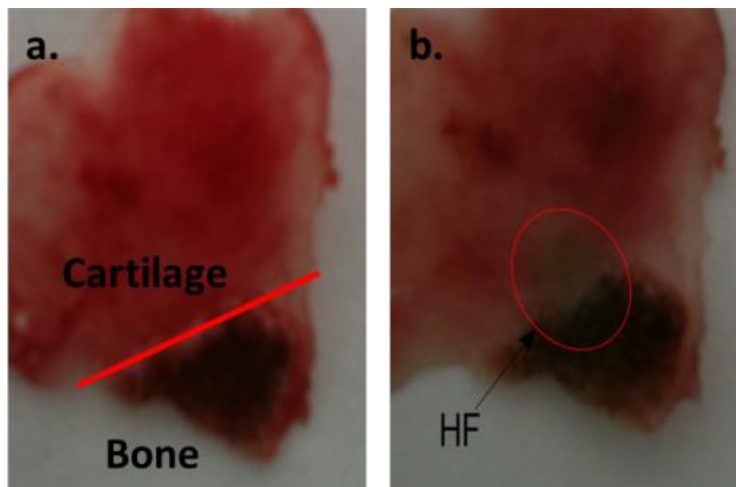


Figure 46. a) Tissue before burn and b) Tissue after HF exposure.

For the undamaged tissue sample, the sample was mounted using the same procedure and conditions as the formalin fixed samples in previous sections. After the image was complete, the tissue was exposed to 48% aqueous HF in an identical manner to the fixed sample. That is, using the same exposure conditions, centering the damage site to include both tissue types, and performing a DI water rinse before re-drying the tissue with compressed nitrogen. As with all other experiments, the slight green discoloration of the tissue in Figure 46b indicates the HF

exposure site. Unlike previous samples, it was noted that although the thickness did not change, a reduction in weight of 9.69 mg was observed after the HF exposure. This nature of this weight reduction remains ambiguous and may be attributed to either the damage incurred from the HF exposure or a slight decay of the sample due to the lack of fixation.

An image 18mm x 18mm was acquired with a pixel pitch of 0.5mm and a time domain window of 18ps was acquired for the sample before HF exposure. The image acquired after exposure was slightly larger, 20mm x 20mm, however the increased area of the image consists chiefly of space outside sample and therefore does not affect the image analysis. An additional image was obtained several days after these two images. The sample was removed and placed in cold storage between these last two images; it was also re-dried with compressed nitrogen before being mounted in the spectrometer. There were no appreciable changes in the resulting reconstruction when compared to the second image indicating that the sample was stable and that a direct comparison between the before and after burn images can be made.

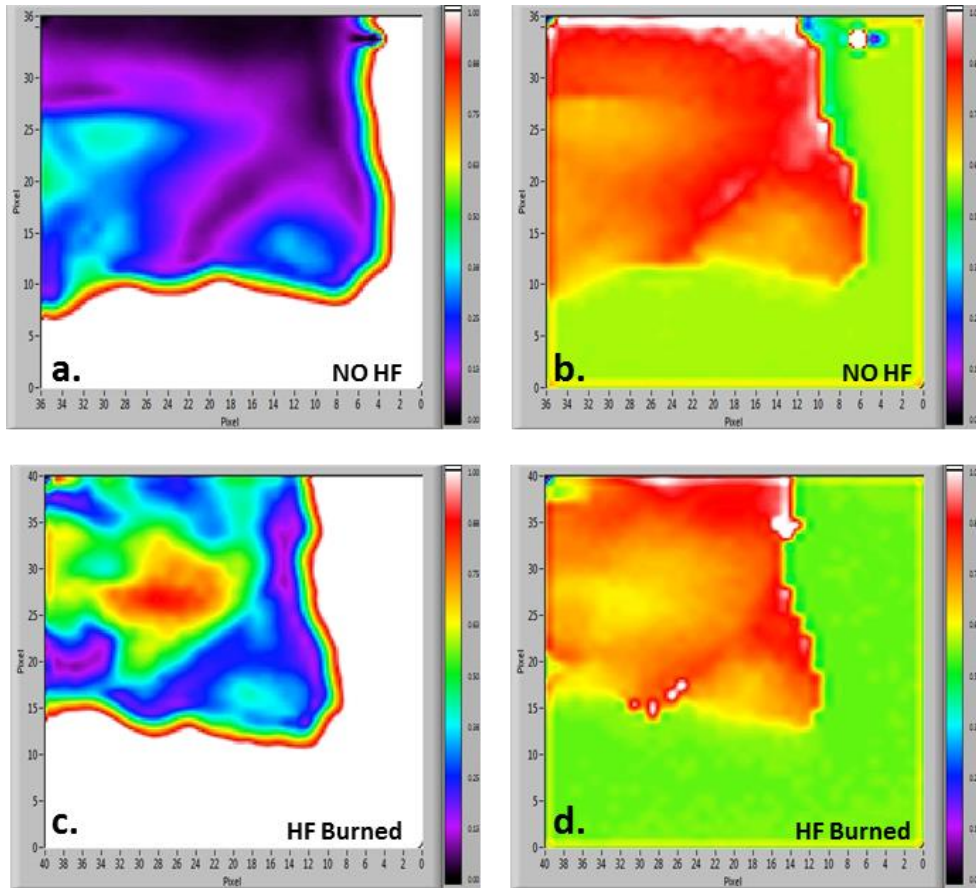


Figure 47. a) before burn TD peak, b) before burn delay, c) after HF TD peak, and d) after HF delay.

The figures above depicts the basic time domain reconstructions for the before and after HF exposure images. The top left (Figure 47a) represents the time domain peak amplitude of the tissue before HF exposure and the top right (Figure 47b) is the propagation delay of the same. The bottom two (Figure 47c&d) are the corresponding image reconstructions for the sample after the structural damage has occurred. A drastic increase in the transmission of THz through both tissue types is exhibited for each case in the location corresponding to acid exposure. Observation of the propagation delay images (Figure 47 b&d) does reveal the expected trend of decreased delay in the burned region. Beyond this, however, the image tells little else about the sample.

Pixel spectrum investigation was performed for representative pixels of each region using the in-built pixel analysis tools in the analyzer software. Inspection of this response reveals a transmission increase of 2.5 times through the damaged tissue, which agrees well with the expectation that was formed based on the formalin fixed samples. In addition, the transmitted THz through the unburned region near the edge of the sample presents the same response that was observed before acid exposure, further confirming that we do not need to be concerned with tissue decay due to the lack of fixation for this sample.

One result from the before and after comparison that was not observable from previous measurements is that there is a marked difference in the homogeneity of damage between the two tissue types. In the undamaged tissue image, the transmitted peak intensity of THz is highly uniform for both bone and cartilage. After HF exposure, however, the cartilage tissue exhibits a more fractured pattern of varied intensity. The compact bone, on the other hand, shows a more ‘concentric’ increase in transmitted intensity as we approach the center of the burned tissue. This difference is clearly related to the uniformity with which the HF damages the cartilage.

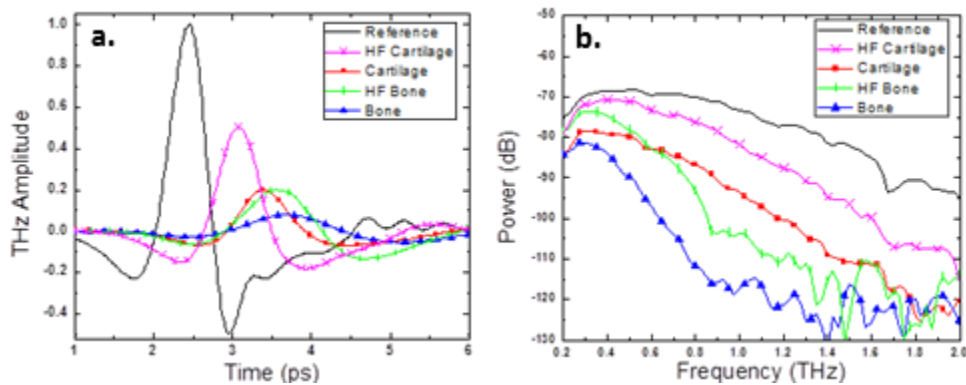


Figure 48. Selected pixel data for a) Time domain b) Frequency Domain before and after HF exposure.

The next figures present frequency domain power reconstructions for 0.45 THz and 0.8 THz (Figure 49). These frequencies were selected based on analysis of the extracted pixel

spectra presented above. For low frequencies (below 0.45 THz) the tissue in the burned region is more transmissive than any undamaged tissue. At 0.45THz (Figure 49c), clear contrast develops between the burned and unburned tissue of a given type; one result that has not been observed in the fixed samples. The transmitted radiation at this frequency for the burned bone is comparable to that of the unburned cartilage resulting from a ‘cross over’ of transmitted power at this frequency which could lead to a false interpretation of the tissue structure if the sample is not known and broadband analysis is not employed.

For frequencies above 0.7 THz and below 1.4 THz (where the all bone tissue falls below the noise threshold) a distinct separation in transmitted power for each region is apparent. In this frequency range, however, the HF exposed tissue is no longer the most transparent due to the sharp fall off of the power spectrum associated with the exposed bone. Figure 49d illustrates the reconstruction at a frequency of 0.8THz which falls within this range of this behavior.

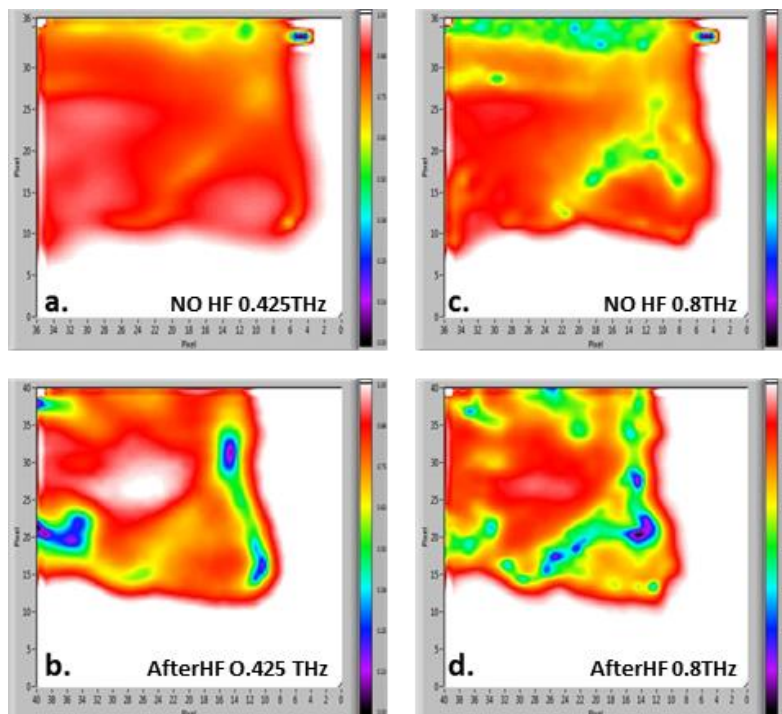


Figure 49. Power Spectrum images of a) non-burned, b) burned tissue at 0.425 THz; and for c) non-burned, d) burned tissue at 0.8THz.

6.3.3 Comparison of Results from Fixation

When the formalin fixed tissue is compared to the freshly cut tissue the contrast developed in the time domain amplitude image is not as strong, although the burn is still evident. One observation that clearly develops is that, by comparing the spectroscopic data in the un-fixed sample to that of the formalin fixed sample, the un-burned cartilage becomes more transparent to the THz radiation after fixation. This results in a smaller contrast between the damaged and undamaged cartilage, where the transmission intensity in the HF burned region only increases by 50%. This would seem to suggest that the formalin is more effective at fixing the tissue which has not been exposed to acid. This observation correlates well with the understanding that the damaged protein strains would cross-link less completely. It should be also noted that the time delay difference between the acid burned and unburned areas is very close for all samples. For example, there is exactly a 0.5ps delay difference between the HF exposed cartilage and unburned cartilage. This shows that the difference in propagation delay is the same independent of fixation, and additionally confirms that the acid damages the tissue structure in a way that can be probed in THz time domain signal.

Comparison of the frequency spectra for the fixed and un-fixed tissue samples shows that the fixed tissue exhibits less distinct slopes for each spectrum than were observed in the un-fixed tissue. The power spectra appear to be ‘compressed’ towards the noise threshold and although the relative intensities are retained qualitatively for each tissue type, identification becomes more difficult due to a lack of overall separation. This observation is clearly indicated in the frequency domain image reconstructions.

From these results, it is clear that a significant reduction in spectroscopic information

occurs when the histological process is applied to the tissue. Not only is the overall deprecation of contrast (expected based on the results from [92]) significant, but damage response information unique to the cartilage tissue is lost. The burns are still observable, but these results suggest that formalin fixation should not be applied in all cases if accurate THz-TDS information is desired.

CHAPTER 7: CONCLUSION

In this work, the tools and methodologies for THz spectroscopic image reconstruction have been explored. The basic experimental method for time domain waveform acquisition and analytical techniques for performing the Fast Fourier Transform used with this system were presented. Next, the physically significant reconstruction criteria were identified in both the time and frequency domain. A LabVIEW-based toolkit for reconstructing the spectroscopic images obtained with our THz-TDS was developed, highlighting the methods of loading, enhancing, and reconstructing images was presented.

Once the methodological basis for acquisition and reconstruction were detailed, several images were taken. The first was of a memory microchip, and was used to demonstrate the application of reconstruction techniques to develop contrast when the basic nature of the sample is known, but in-depth spectroscopic analysis of the materials contained within have not been performed prior to imaging. This allowed us to evaluate the validity of several reconstruction techniques and use them to enhance the overall understanding of the effects that different materials have on the THz propagation.

The next study presented, the osseous tissue, begins by showing the opposite case, when baseline spectroscopic responses have been obtained for complex tissue structures. By reconstructing from these observed spectroscopic responses, the merits of using such baselines in a complex tissue sample were evaluated. We observed from this that a thorough understanding of the homogeneity of the select tissues is critical when designing analysis around single baselines. After basic tissue identification was achieved, a study in several parts on the effects of structural damage to osseous tissue was performed.

For this damage study, we clearly show that distinct contrast can be developed based on exposure intensity to HF. In addition, the responses of different osseous tissue types were characterized. The final step of this study found that the use of formalin for the preparation of osseous tissue samples can significantly impact the depth of information attainable, and should not be used indiscriminately in all cases.

Contrast was achieved for all samples with varying levels of detail. Clear contrasts were not obtained as expected for all reconstruction techniques, however, further analysis based on these reconstructions allowed for a clearer insight into each sample presented. Based on these results, we found that the methodologies for images reconstruction and criteria selection are valid and that we are capable of performing detailed reconstructions with this tool that accurately represent the physical interactions between THz radiation and any sample that is chosen for imaging.

REFERENCES

- [1] S. Balci, W. Baughman, D. S. Wilbert, G. Shen, P. Kung, S. M. Kim, "Characteristics of THz carrier dynamics in GaN thin film and ZnO nanowires by temperature dependent terahertz time domain spectroscopy measurement," *Solid-State Elect.* **78**, 68-74 (2012).
- [2] S. M. Kim, W. Baughman, D. S. Wilbert, L. Butler, M. Bolus, S. Balci, and P. Kung, "High sensitivity and high selectivity terahertz biomedical imaging (Invited Paper)," *Chin. Opt. Lett.* **9**, (2011).
- [3] W. E. Baughman, D. S. Wilbert, S. Balci, M. Bolus, M. Baker, P. Kung, S. M. Kim, M. S. Heimbeck, H. O. Everitt, "Comparative reconstructions of THz spectroscopic imaging for non-destructive testing and biomedical imaging," *Terahertz Physics, Devices, and Systems VI: Advanced Applications in Industry and Defense, Proc. SPIE 8363*, 83630W (2012).
- [4] H. Yokus, W. Baughman, S. Balci, M. Bolus, D. S. Wilbert, P. Kung, S. M. Kim, "Identification of tissue interaction of terahertz radiation toward functional tissue imaging," *Terahertz and Ultrashort Electromagnetic Pulses for Biomedical Applications, Proc. SPIE 8585*, 85850K (2013).
- [5] M. P. Hokmabadi, D. S. Wilbert, P. Kung, S. M. Kim, "Design and analysis of perfect terahertz metamaterial absorber by a novel dynamic circuit model," *Opt. Express* **21**, 16455-16465 (2013).
- [6] D. S. Wilbert, M. P. Hokmabadi, W. Baughman, P. Kung, S. M. Kim, "Highly efficient, polarization insensitive terahertz metamaterial perfect absorber and imaging," *Photonics Conference (IPC), 2012 IEEE* , pp.228-229 (2012)
- [7] D. S. Wilbert, M. P. Hokmabadi, J. Martinez, P. Kung, S. M. Kim, "Terahertz metamaterials perfect absorbers for sensing and imaging," *Terahertz and Ultrashort Electromagnetic Pulses for Biomedical Applications, Proc. SPIE 8585*, 85850Y (2013).
- [8] L. Butler, D. S. Wilbert, W. Baughman, S. Balci, P. Kung, S. M. Kim, M. S. Heimbeck, H. O. Everitt, "Design, simulation, and characterization of THz metamaterial absorber," *Terahertz Physics, Devices, and Systems VI: Advanced Applications in Industry and Defense, Proc. SPIE 8363*, 83630J (2012).
- [9] M. F. Kimmitt, "Restrahlen to T-rays – 100 years of terahertz radiation," *J. of Bio. Phys.* **29**, 77-85 (2003).
- [10] H. Rubens, B. W. Snow, "On the Refraction of Rays of Great Wavelength in Rock Salt, Sylvine, and Fluorite," *Phil. Mag.* **35**, 35-45 (1893).
- [11] S. Dexheimer, *Terahertz Spectroscopy: Principles and Applications*. Boca Raton, FL: CRC Press, 2008.

- [12] C. Sirtori, "Applied physics: Bridge for the terahertz gap," *Nature* **417**, no. 6855, 132-133 (2002).
- [13] X. Zhang, J. Xu, Introduction to THz wave photonics. Springer Publishing Company, Incorporated, 2010.
- [14] E. F. Barker, W. W. Selator, "The Infrared Spectrum of Heavy Water," *J. Chem. Phys.* **3**, 660 (1935).
- [15] E. F. Nichols, J. D. Tear, "Short Electric Waves," *Phys. Rev.* **21**, 587-610 (1923).
- [16] Y. S. Lee, Principles of terahertz science and technology. Springer Publishing Company, Incorporated, 2008.
- [17] A. Rostami, H. Rasooli, H. Baghban, Terahertz Technology: Fundamentals and Applications, Springer Publishing Company, Incorporated, 2011.
- [18] B. Ferguson, X.-C. Zhang, "Materials for terahertz science and technology," *Nature Mater.* **1**, 26-33 (2002).
- [19] D. H. Auston, K. P. Cheung, J. A. Valdmanis, D. A. Kleinman, "Cherenkov radiation from femtosecond optical pulses in electro-optic media," *Phys. Rev. Lett.* **53**, no. 16, 1555-1558 (1984).
- [20] N. Katzenellenbogen, D. Grischkowsky, "Efficient generation of 380 fs pulses of THz radiation by ultrafast laser pulse excitation of a biased metal semiconductor interface," *Appl. Phys. Lett.* **58**, no. 3, 222-224 (1991).
- [21] B. B. Hu, X.-C. Zhang, D. H. Auston, P. R. Smith, "Free-space radiation from electrooptic crystals," *Appl. Phys. Lett.* **56**, no. 6, 506-508 (1990).
- [22] Ch. Fattinger, D. Grischkowsky, "Terahertz beams," *Appl. Phys. Lett.* **54**, no. 6, 490-492 (1989).
- [23] P. Shumyatsky, R. R. Alfano, "Terahertz sources," *J. Biomed. Opt.* **16**, no. 3 (2011).
- [24] P. R. Smith, D. H. Auston, M. C. Nuss, "Subpicosecond photoconducting dipole antennas," *IEEE J. Quantum Electron.* **24**, no. 2, 255-260 (1988).
- [25] T. A. Liu, R. H. Chou, C. L. Pan, "Dependence of terahertz radiation on gap sizes of biased multi-energy arsenic-ion-implanted and semi-insulating GaAs antennas," *App. Phys. B* **95**, 739-744 (2008).
- [26] J. T. Darrow, X. Zhang, D. H. Auston, "Saturation properties of large-aperture photoconducting antennas," *IEEE J. Of Quantum Elec.* **28**, no. 6, 1607-1616 (1992).
- [27] P. K. Benicewicz, J. P. Roberts, A. J. Taylor, "Scaling of terahertz radiation from large-aperture biased photoconductors," *J. Opt. Soc. Am. B* **11**, no. 12 (1994).

- [28] J. H. Kim, A. Polley, S. E. Ralph, "Efficient photoconductive terahertz source using line excitation," *Opt. Lett.* **30**, no. 18, 2490-2492 (2005).
- [29] M. Tani, S. Matsuura, K. Sakai, S. Nakashima, "Emission characteristics of photoconductive antennas based on low-temperature-grown GaAs and semi-insulating GaAs." *Appl. Opt.* **36**, no. 30 (1997).
- [30] M. Suzuki, H. Ohtake, T. Hirosumi, K. Fujii, M. Tonouchi, "Terahertz emissions from semiconductors excited by femtosecond pulses at wavelengths of 1560, 1050, and 780nm." *Conf. Lasers and Electro-Optics, JTuD25.* (OSA, 2006).
- [31] D. H. Auston, M. C. Nuss, "Electrooptic generation and detection of femtosecond electrical transients," *IEEE Journ. Quant. Electron.* **24**, no. 2 (1988).
- [32] J. T. Darrow, B. B. Hu, X.-C. Zhang, D. H. Auston, "Subpicosecond electromagnetic pulses from large-aperture photoconducting antennas," *Opt. Lett.* **15**, no. 6, 323-325 (1990).
- [33] A. G. Davies, E. H. Linfield, M. B. Johnston, "The development of terahertz sources and their applications," *Phys. Med. Biol.* **47**, 3679-3689 (2002).
- [34] N. van der Valk, T. Wenckebach, P. Planken, "Full mathematical description of electro-optic detection in optically isotropic crystals," *J. Opt. Soc. of Am. B* **21**, no. 3 (2004).
- [35] J. B. Jackson, M. Mourou, J. F. Whitaker, I. N. Duling III, S. L. Williamson, M. Menu, G. A. Mourou, "Terahertz imaging for nondestructive evaluation of mural paintings," *Opt. Commun.* **281**, 527-532 (2008).
- [36] DOE-NSF-NIH Workshop on "Opportunities in THz Science", Arlington, VA, February 12-14, 2004.
- [37] P.H. Siegel, "Terahertz technology," *IEEE Trans. Microw. Theory Tech.* **50**, no. 3, 910-918 (2002).
- [38] P.H. Siegel, "Terahertz technology in biology and medicine," *IEEE Trans. Microw. Theory Tech.* **52**, no. 10, 2438-2447 (2004).
- [39] L. Duvillaret, F. Garet, J.-L. Coutaz, "A reliable method for extraction of material parameters in terahertz time-domain spectroscopy", *IEEE J. of Selec. Top. In Quant. Electro.* **2**, no. 3, 739-746 (1996).
- [40] L. Duvillaret, F. Garet, J.-L. Coutaz, "Highly Precise Determination of Optical Constants and Sample Thickness in Terahertz Time-Domain Spectroscopy," *Appl. Opt.* **38**, 409-415 (1999).
- [41] F. Wang, J. Shan, E. Knoesel, M. Bonn, T. F. Heinz, "Electronic charge transport in sapphire studied by optical pump THz probe spectroscopy," *Proc. SPIE 5352*, no. 216 (2004).

- [42] T. D. Dorney, R. G. Baraniuk, D. M. Mittleman, "Material parameter estimation with terahertz time-domain spectroscopy," *J. Opt. Soc. Am. A* **18**, 1562-1571 (2001).
- [43] N. Laman, S. Harsha, D. Grischikowsky, J. Mellinger, "High Resolution Waveguide THz Spectroscopy of Biological Molecules," *Biophys. J.* **94**, 1010-1020 (2008).
- [44] A. G. Davies, E. H. Linfield, M. B. Johnston, "The development of terahertz sources and their applications," *Phys. Med. Biol.* **47**, 3679-3689 (2002).
- [45] N. Krumbholz, K. Gerlach, F. Rutz, M. Koch, R. Piesiewicz, T. Kürner, D. Mittleman, "Omnidirectional terahertz mirrors: A key element for future terahertz communication systems." *Appl. Phys. Lett.* **88**, 202905 (2006).
- [46] J.-S. Rieh; B. Jagannathan, D. R. Greenberg, M. Meghelli, A. Rylyakov, F. Guarin, Z. Yang, D. C. Ahlgren, G. Freeman, P. Cottrell, D. Haramé, "SiGe heterojunction bipolar transistors and circuits toward terahertz communication applications," *IEEE Trans. on Microwave Theory and Techniques* **52**, no.10, 2390-2408 (2004).
- [47] R. Piesiewicz, M. N. Islam, M. Koch, T. Kurner, "Towards Short-Range Terahertz Communication Systems: Basic Considerations," *Applied Electromagnetics and Communications, 2005. ICECom 2005. 18th International Conference on*, 1-5, (2005).
- [48] I. C. Mayorga, A. Schmitz, T. Klein, C. Leinz, R. Gusten, "First In-Field Application of a Full Photonic Local Oscillator to Terahertz Astronomy," *IEEE Trans. on Terahertz Science and Technology* **2**, no.4, 393-399, (2012).
- [49] P. H. Siegel, "THz Instruments for Space," *IEEE Trans. on Antennas and Propagation* **55**, no.11, 2957-2965 (2007).
- [50] E. Heinz, T. May, G. Zieger, D. Born, S. Anders, G. Thorwirth, V. Zakosarenko, M. Schubert, T. Krause, M. Starkloff, A. Krüger, M. Schulz, F. Bauer, H.-G. Meyer, "Passive Submillimeter-wave Stand-off Video Camera for Security Applications," *J. Infrared Milli. Terahz. Waves* **31**, 1355-1369 (2010).
- [51] D.L. Woolard, E.R. Brown, A.C. Samuels, J.O. Jensen, T. Globus, B. Gelmont, and M. Wolski, "Terahertz-frequency remote-sensing of biological warfare agents," *Microwave Symposium Digest, 2003 IEEE MTT-S International* **2**, no. 763 (2003).
- [52] J.S. Melinger, N. Laman, D. Grischkowsky, "The underlying terahertz vibrational spectrum of explosive solids," *Appl. Phys. Lett.* **93**, no. 011102 (2008).
- [53] M.S. Heimbeck, K.K. Myung, D.A. Gregory, H.O. Everitt, "Terahertz digital holography using angular spectrum and dual wavelength reconstruction methods," *Opt. Exp.* **19**, 9147-9156 (2011).
- [54] A.A. Gowen, C. O'Sullivan, C.P. O'Donnell, "Terahertz time domain spectroscopy and imaging: Emerging techniques for food process monitoring and quality control," *Trends in Food Science & Technology* **25**, no. 1, 40-46 (2012).

- [55] P. F. Taday, “Applications of terahertz spectroscopy to pharmaceutical sciences,” *Phil. Trans. R. Soc. Lond. A* **362**, no. 1815, 351-364 (2004).
- [56] M. A. Flower, *Webb’s Physics of Medical Imaging*, Second Edition. Boca Raton, FL, CRC Press 2012.
- [57] H. Zaidi, *Quantitative Analysis in Nuclear Medicine Imaging*. Springer Science 2006.
- [58] A. Wolbarst, *Looking Within: How X-ray, CT, MRI, Ultrasound, and Other Medical Images are Created, and how They Help Physicians Save Lives*. University of California Press, 1999.
- [59] A. K. Louis, “Medical Imaging: state of the art and future development,” *Inverse Problems* **8**, 709, (1992).
- [60] D. Plusquellic, K. Siegrist, E. Heilweil, O. Esenturk. “Applications of Terahertz Spectroscopy in Biosystems,” *Chem. Phys. Chem.* **8**, 2412 – 2431, (2007).
- [61] A. Momose, T. Takeda, Y. Itai, K. Hirano, “Phase-contrast X-ray computed tomography for observing biological soft tissues,” *Nat. Med.* **2**, 473-475 (1996).
- [62] A. Pietrobelli, Z. Wang, C. Formica, S. Heymsfield, “Dual-energy X-ray absorptiometry: fat estimation errors due to variation in soft tissue hydration,” *Am. J. of Physio. – Endo. and Metab.* **274**, E808-E816 (1998).
- [63] T. Donath, F. Pfeiffer, O. Bunk, C. Grunzweig, E. Hempel, S. Popescu, P. Vock, C. David, “Toward Clinical X-ray Phase-Contrast CT: Demonstration of Enhanced Soft-Tissue Contrast in Human Specimen,” *Invest. Radiology* **45**, no. 7, 445-452, (2010).
- [64] Q.-Y. Cai, S. H. Kim, K. S. Choi, S. Y. Kim, S. J. Byun, K. W. Kim, S. H. Park, S. K. Juhng, K.-H. Yoon, “Colloidal Gold Nanoparticles as a Blood-Pool Contrast Agent for X-ray Computed Tomography in Mice,” *Invest. Radiology* **42**, no. 12, 797-806, (2007).
- [65] A. G. Markelz, A. Roitberg, E. J. Heilweil, “Pulsed terahertz spectroscopy of DNA, bovine serum albumin and collagen between 0.06 to 2.00 THz,” *Chem. Phys. Lett.* **320**, 42-48 (2000).
- [66] M. Brucherseifer, M. Nagel, P. H. Bolívar, H. Kurz, A. Bosserhoff, R. Büttner, “Label-free probing of the binding state of DNA by time-domain terahertz sensing,” *Appl. Phys. Lett.* **77**, no. 24, 4049-4051 (2000).
- [67] A. Markelz, S. Whitmire, J. Hillebrecht, R. Birge, “Terahertz time domain spectroscopy of biomolecular conformational modes,” *Phys. Med. Biol.* **47**, 3797-3805 (2002).
- [68] K. Yamamoto, K. Tominaga, H. Sasakawa, A. Tamura, H. Murakami, H. Ohtake, N. Sarukura, “Far-infrared absorption measurements of polypeptides and cytochrome c by THz radiation,” *Bull. Chem. Soc. Japan* **75**, 1083–1092 (2002).

- [69] S. E. Whitmire, D. Wolpert, A. G. Markelz, J. R. Hillebrecht, J. Galan, R. R. Birge, "Protein flexibility and conformational state: A comparison of collective vibrational modes of wild-type and D96N bacteriorhodopsin," *Biophys. J.* **85**, 1269–1277 (2003).
- [70] P. H. Bolívar, M. Nagel, F. Richter, M. Brucherseifer, H. Kurz, A. Bosserhoff, R. Büttner, "Label-free THz sensing of genetic sequences: Towards 'THz biochips'," *Phil. Trans. R. Soc. Lond. A* **362**, 323-335 (2004).
- [71] B. M. Fischer, M. Hoffmann, H. Helm, R. Wilk, R. Rutz, T. Kleine-Ostmann, M. Kock, P. U. Jepsen, "Terahertz time-domain spectroscopy and imaging of artificial RNA," *Opt. Exp.* **13**, 5206-5215 (2005).
- [72] J.-Y. Chen, J. R. Knab, J. Cerne, A. G. Markelz, "Large oxidation dependence observed in terahertz dielectric response for cytochrome C," *Phys. Rev. E. Rapid* **72**, no. 04090, 1-4 (2005).
- [73] A. G. Markelz, J. R. Knab, J. Y. Chen, Y. He, "Protein dynamical transition in terahertz dielectric response," *Chem. Phys. Lett.* **442**, 413-417 (2007).
- [74] J.-Y. Chen, J. R. Knab, S. Ye, Y. He, A. G. Markelz, "Terahertz dielectric assay of solution phase protein binding," *Appl. Phys. Lett.* **90**, no. 243901, 1-3 (2007).
- [75] J. Knab, J.-Y. Chen, A. Markelz, "Hydration dependence of conformational dielectric relaxation of lysozyme," *Biophys. J.* **90**, 2576-2581 (2006).
- [76] C. Kistner, A. Andre, T. Fischer, A. Thoma, C. Janke, A. Bartels, T. Gisler, G. Maret, T. Dekorsy, "Hydration dynamics of oriented DNA films investigated by time-domain terahertz spectroscopy," *Appl. Phys. Lett.* **90**, no. 233902, 1-3 (2007).
- [77] B.B. Hu, M. C. Nuss, "Imaging with Terahertz Waves," *Opt. Lett.* **20**, no. 16, 1716-1718 (1995).
- [78] T. Kleine-Ostmann, P. Knobloch, M. Koch, S. Hoffmann, M. Breebe, M. Hofmann, G. Hein, K. Pierz, M. Sperling, K. Donhuijsen, "Continuous-wave THz Imaging," *Elect. Lett.* **37**, no. 24 (2001).
- [79] R. M. Woodward, B. E. Cole, V. P. Wallace, R. J. Pye, D. D. Arnone, E. H. Linfield, M. Pepper, "Terahertz pulse imaging in reflection geometry of human skin cancer and skin tissue," *Phys. in Med. And Bio.* **47**, no. 21 (2002).
- [80] M. A. Brun, F. Formanek, A. Yasuda, M. Sekine, N. Ando, Y. Eishii, "Terahertz imaging applied to cancer diagnosis," *Phys. Med. Biol.* **55**, no. 4615 (2010).
- [81] S. Nakajima, H. Hoshina, M. Yamashita, C. Otani, N. Miyoshi, "Terahertz imaging diagnostics of cancer tissues with a chemometrics technique," *App. Phys. Lett.* **90**, no. 041102 (2007).

- [82] P. C. Ashworth, E. Pickwell-MacPherson, E. Provenzano, S. E. Pinder, A. D. Purushotham, M. Pepper, V. P. Wallace, "Terahertz pulsed spectroscopy of freshly excised human breast cancer," *Opt. Express* **17**, 12444-12454 (2009).
- [83] S. J. Oh, J. Kang, I. Maeng, J.-S. Suh, Y.-M. Huh, S. Haam, J.-H. Son, "Nanoparticle-enabled terahertz imaging for cancer diagnosis," *Opt. Exp.* **17**, 3469-3475 (2009).
- [84] P.C. Ashworth, P. O'Kelly, A.D. Purushotham, S.E. Pinder, M. Kontos, M. Pepper, V.P. Wallace, "An intra-operative THz probe for use during the surgical removal of breast tumors," *Infrared, Millimeter and Terahertz Waves, 2008. IRMMW-THz 2008. 33rd International Conference on*, 1-3 (2008).
- [85] J. Ryu, Y. Jung, S. Baek, J. Lee, S. Kim, S. Kwon, J. Kim, "Diagnosis of Dental Cavity and Osteoprosis Using Terahertz Transmission Images," *Springer Series in Chemical Physics* **66**, 265-267 (2001).
- [86] E. Pickwell, V. P. Wallace, B. E. Cole, S. Ali, C. Longbottom, R. J. M. Lynch, and M. Pepper, "A Comparison of Terahertz Pulsed Imaging with Transmission Microradiography for Depth Measurement of Enamel Demineralization in vitro," *Caries Research* **41**, no. 1 (2007).
- [87] Y. C. Sim, I. Maeng, J.-H. Son, "Frequency-dependent characteristics of terahertz radiation on the enamel and dentin of human tooth," *Curr. Appl. Phys.* **9**, no. 5, 946-949 (2009).
- [88] M. Hirmer, S. N. Danilov, S. Giglberger, J. Putzger, A. Niklas, A. Jäger, K.-A. Hiller, S. Löffler, G. Schmalz, B. Redlich, I. Schulz, G. Monkman, S. D. Ganichev, "Spectroscopic Study of Human Teeth and Blood from Visible to Terahertz Frequencies for Clinical Diagnosis of Dental Pulp Vitality," *J. Infrared Milli Terahz Waves* **33**, 366-375 (2012).
- [89] M. R. Stringer, D. N. Lund, A. P. Foulds, A. Uddin, E. Berry, R. E. Miles, A. G. Davies, "The analysis of human cortical bone by terahertz time-domain spectroscopy", *Phys. Med. Biol.* **50**, 3211-3219 (2005).
- [90] W.C Kan W.-S. Lee, W.-H. Cheung, V. P. Wallace, E. Pickwell-MacPherson, "A pilot study of terahertz pulsed imaging of osteoarthritis," *IRMMW-THz 2008. 33rd International Conference on*, 1-2 (2008).
- [91] W.C Kan W.-S. Lee, W.-H. Cheung, V. P. Wallace, E. Pickwell-MacPherson, "Terahertz pulsed imaging of knee cartilage," *Biomed. Opt. Express* **1**, no. 3, 967-974 (2010).
- [92] M. Bessou, B. Chassagne, J.-P. Caumes, C. Pradère, P. Maire, M. Tondusson, E. Abraham, "Three-dimensional terahertz computed tomography of human bones," *Appl. Opt.* **51**, 6738-6744 (2012).
- [93] S. Yiwen, E. Pickwell-MacPherson, "The effects of formalin fixing on terahertz properties of biological samples," *IRMMW-THz 2008. 33rd International Conference*, 1-2 (2008).

- [94] N. C. J. van der Valk, T. Wenckebach, P. C. M. Planken, "Full mathematical description of electro-optic detection in optically isotropic crystals," *J. Opt. Soc. Am. B* **21**, 622-631 (2004).
- [95] M. van Exter, C. Fattinger, D. Grischkowsky, "Terahertz time-domain spectroscopy of water vapor," *Opt. Lett.* **14**, 1128-1130 (1989).
- [96] Y. Shen, P. Taday, "Development and application of terahertz pulsed imaging for nondestructive inspection of pharmaceutical tablet," *IEEE J. of Sel. Topics. Quantum Electron.* **14**, no. 2, 407-415 (2008).
- [97] M. Mizuno, K. Fukunaga, S. Saito, I. Hosako, "Analysis of calcium carbonate for differentiating between pigments using terahertz spectroscopy," *J. of the Euro. Opt. Soc. Rap. Pub.* **4**, no. 09044 (2009).